



Universidade do Minho

Escola de Engenharia

Tomás Torres Martins

Development of a 3-axis MEMS Magnetometer based on Lorentz Force

October 2022



Universidade do Minho

Escola de Engenharia

Tomás Torres Martins

**Development of a 3-axis MEMS
magnetometer based on Lorentz force**

Master Thesis

Masters in physics engineering

Devices, Microsystems and Nanotechnologies

Trabalho efetuado sob a orientação de

Dra. Rosana Maria Alves Dias

**Professor Dr. João Pedro dos Santos Hall Agorreta
de Alpuim**

October 2022

COPYRIGHTS AND TERMS OF USE OF WORK BY THIRD PARTIES

This is an academic work that can be used by third parties as long as the internationally accepted rules and good practices are respected, concerning copyright and related rights.

Thus, this work can be used under the terms set out in the license below.

If the user needs permission to be able to make use of the work under conditions not provided for in the indicated license, he must contact the author, through the RepositóriUM of the University of Minho.

License granted to users of this work



Atribuição

CC BY-NC

<https://creativecommons.org/licenses/by-nc/4.0/>

ACKNOWLEDGEMENTS

First and foremost, a big thank you to my supervisor Dr. Rosana Dias for the opportunity to embrace this project and the patience, guidance, and availability to help me throughout my master's dissertation. I'd also like to thank Professor Pedro Alpuim for his commitment to my project and allowing me to work with a fantastic group of people from the 2DMD Group who helped me through the good and the bad times of my thesis keeping my motivation and caffeine intake on the high note. I also thank all the people from the IMiNa group that supported me with a special thank you to Inês Garcia who was always available to answer my questions.

I would also like to thank my friends from the physics and physics engineering course with whom I shared moments that I will never forget with the hopes that these friendships last for a lifetime.

Finally, I want to thank my girlfriend Telma, the person most responsible for pulling me from the hard times and, at times, believing more in me than myself. And to my parents, Mario and Geraldina, as well as my brothers, Vasco and Lucas, my gratitude for the unconditional support and love that they gave me. My voyage through physics was rough and mentally exhausting but I wouldn't replace the moments that I spent at UMinho for anything. To all who supported me through this quest and from the bottom of my heart: Thank you.

This work was framed in the scope of the Project (Link4S)ustainability - A new generation connectivity system for creation and integration of networks of objects for new sustainability paradigms [POCI-01-0247-FEDER-046122 | LISBOA-01-0247-FEDER-046122], financed by the Operational Competitiveness and Internationalization Programmes COMPETE 2020 and LISBOA 2020, under the PORTUGAL 2020 Partnership Agreement, and through the European Structural and Investment Funds in the FEDER component

Cofinanciado por:



LINK4S

STATEMENT OF INTEGRITY

I hereby declare having conducted this academic work with integrity. I confirm that I have not used plagiarism or any form of undue use of information or falsification of results along the process leading to its elaboration.

I further declare that I have fully acknowledged the Code of Ethical Conduct of the University of Minho

Terêncio Torres Martins

ABSTRACT

Typical **magnetometers** found in the magnetic fields research are highly incompatible with the massive **MEMS** technology industry that has been the object of study in the past years. This aspect leads to the rapid increase in production costs and reliability reduction. Furthermore, most of the magnetometers that are adapted to this technology are highly complex and with little to no adaptation to outer-space research. In this work, a novel single-axis MEMS magnetometer based on the principle of the **Lorentz force** capable of reading fields in the X or Y direction is designed and simulated with the description of a fabrication method to be used. This magnetometer uses an innovative design for a current-carrying-bar that's highly adaptable to a variety of scenarios with a low 100Ω current resistance in each of its paths. An amplitude-modulated method is approached through the use of a **capacitive-readout** system and an **off-resonance** frequency of operation to achieve the detection baseline of a 1aF capacitive variation at a 20nT magnetic field. This involves the use of various mechanisms to increase the quality factor and reduce the overall stiffness of the device to increase its displacement caused by the Lorentz force. The device is also to be operated at a 500Pa atmosphere to reduce the damping and, at the same time, increase the quality factor. A thermomechanical noise below $3 \text{ nT}/\sqrt{\text{Hz}}$ with a frequency of operation at around 4977 Hz was deemed necessary to adapt the design to another previously designed single-axis MEMS magnetometer capable of reading fields in the Z direction.

Various simulation and design tools are used to predetermine the best properties at which the magnetometer will be operated to its highest capabilities. Through these simulations, a 50Hz bandwidth magnetometer, required for spatial research, is achieved with a capacitance variation of 1.37aF at 20nT surpassing the initial requirements. A $1.77 \text{ nT}/\sqrt{\text{Hz}}$ thermomechanical noise is obtained, well below the baseline that was defined for this work.

A fabrication layout was developed with all lithography masks designed, and a microfabrication process flow was devised. The microfabrication process run was partially completed and it's still ongoing.

Keywords: magnetometers, MEMS, Lorentz force, capacitive-readout, off-resonance.

RESUMO

Os **magnetômetros** típicos encontrados na investigação de campos magnéticos são altamente incompatíveis com a enorme indústria da tecnologia **MEMS** que tem sido objeto de estudo nos últimos anos. Este aspeto leva ao rápido aumento dos custos de produção e à redução da fiabilidade. Para além disso a maioria dos magnetômetros adaptados a esta tecnologia são altamente complexos e com pouca ou nenhuma adaptação à investigação espacial.

Neste trabalho, um novo magnetómetro MEMS de um único eixo baseado no princípio da **força de Lorentz** capaz de ler campos na direção X ou Y é concebido e simulado com a descrição de um método de fabrico a ser utilizado. Este magnetómetro utiliza um desenho inovador para uma barra condutora que é altamente adaptável a uma variedade de cenários com uma baixa resistência de 100Ω em cada um dos seus caminhos. Um método de modulação em amplitude é abordado através da utilização de um sistema de **leitura capacitiva** e uma frequência de operação com um **desvio da ressonância** para alcançar a linha de base de deteção de uma variação capacitiva de 1aF para um campo magnético de 20nT. Isto envolve a utilização de vários mecanismos para aumentar o fator de qualidade e reduzir a rigidez geral do dispositivo para aumentar o deslocamento causado pela força de Lorentz. O dispositivo deve também ser operado a uma atmosfera de 500Pa para reduzir o amortecimento e, ao mesmo tempo, aumentar o factor de qualidade. Um ruído termomecânico inferior a $3\text{ nT}/\sqrt{\text{Hz}}$ com uma frequência de operação de cerca de 4977 Hz foram consideradas necessárias para adaptar o desenho a outro magnetómetro MEMS de um eixo, previamente concebido, capaz de ler campos na direção Z.

Várias ferramentas de simulação e desenho são utilizadas para pré-determinar as melhores propriedades em que o magnetómetro será operado até às suas capacidades mais elevadas. Através destas simulações, um magnetómetro de 50Hz de largura de banda, necessário para a investigação espacial, é alcançado com uma variação de capacidade de 1.37aF a 20nT, ultrapassando os requisitos iniciais. É obtido um ruído termomecânico de $1.77\text{ nT}/\sqrt{\text{Hz}}$, bem abaixo da linha de base que foi definida para este trabalho.

Foi desenvolvido um esquema de fabricação com todas as máscaras litográficas concebidas, e foi concebido um fluxo de processo de microfabricação. A execução do processo de microfabricação foi parcialmente concluída e ainda está em curso.

Palavras-chave: magnetómetros, MEMS, força de Lorentz, leitura capacitiva, desvio da ressonância.

INDEX

Copyrights and terms of use of work by third parties	i
Acknowledgements.....	ii
Abstract.....	iv
Resumo.....	v
Index.....	vi
Figure Index	ix
Table Index.....	xii
List of Abbreviations, initials, and, acronyms	xiii
1. Introduction	1
2. MEMS Magnetometry.....	3
2.1 MEMS Technology.....	3
2.1.1 MEMS magnetometers	4
2.2 Lorentz force MEMS Magnetometers	5
2.2.1 State of art	5
2.3 Technology comparison.....	7
3. Analytical Model.....	9
3.1 Lorentz Force	9
3.2 Capacitive Readout.....	11
3.3 Increasing the Lorentz Force.....	11
3.4 Bandwidth.....	13
3.4.1 Off-Resonance Operation	14
3.5 Damping Coefficient.....	15
3.5.1 Slide Damping.....	15
3.6 Thermo-mechanical noise.....	17
3.7 Magnetometer target specifications.....	17
4. Design and Simulation	19
4.1 Simulation Tools.....	19

4.2	Current Carrying bar.....	19
4.2.1	Electrical resistance.....	21
4.3	Parallel Plates	22
4.3.1	Plate Thinning	24
4.4	Eigenmode.....	25
4.5	Simulations	26
4.5.1	Early Simulations.....	27
4.5.2	Main structure simulations.....	32
4.6	Final Device	35
5.	Microfabrication	37
5.1	Cleanroom	37
5.2	General microfabrication techniques	38
5.2.1	Lithography	38
5.2.2	Metal deposition and etching	39
5.2.3	Grayscale Lithography.....	40
5.2.4	SiO ₂ deposition and etching	41
5.2.5	Silicon etching	42
5.3	MEMS magnetometer process flow	43
5.3.1	Frontside metal deposition and patterning and SiO ₂ deposition	44
5.3.2	Frontside Grayscale lithography and SiO ₂ etch	45
5.3.3	Backside Lithography and SiO ₂ etch.	46
5.3.4	Frontside Silicon etching.....	46
5.3.5	Backside Silicon etch and release	47
5.4	Layers Design	48
5.4.1	GS1.....	48
5.4.2	GS2.....	49
5.4.3	GS3.....	49
5.4.4	METAL	49
5.4.5	TRENCH.....	50

5.4.6	Complete device	51
5.4.7	Other structures	51
5.4.8	Complete wafer design	52
5.5	Microfabrication results	53
6.	Conclusion and Future work.....	55
	References	56
	Annex I – MATLAB algorithm	63
	Annex II – RUNSHEET	68

FIGURE INDEX

<i>Figure 1. Comparison between different kinds of magnetic sensor technology. Adapted from [30].</i>	<i>7</i>
<i>Figure 2. Before (Top) and after (Bottom) a current is applied to the CCB.</i>	<i>10</i>
<i>Figure 3. Displacement of plates before (left) and after (right) a force is applied.</i>	<i>11</i>
<i>Figure 4. Vibration amplitude vs Frequency due to various quality factors, taken from [42].</i>	<i>12</i>
<i>Figure 5. Bandwidth comparison between resonance and off-resonance operation for two different devices o the first one with a Q of 600 and the second with a Q of 150. Taken from [27].</i>	<i>14</i>
<i>Figure 6. Topology of a slide damper (left). The surface moves tangentially to the surface (right).</i>	<i>16</i>
<i>Figure 7. Simple illustration of a single CCB. It has 3 main components, the Lorentz bar (Blue), the lever-like bars (green) and the springs (red).</i>	<i>20</i>
<i>Figure 8. Top view and cross-section of Parallel plates system. Movable parallel plates (yellow) and fixed plates (orange). The cross-section shows the result of a downward Lorentz force.</i>	<i>22</i>
<i>Figure 9. Capacitor parallel plate structure where movable (yellow) and parallel (orange) plates variables are represented. In this structure, the plate length (PL), plate width (PW), damper length (DL), parallel plate distance (D1) and plate separation (PS) variables are shown.</i>	<i>23</i>
<i>Figure 10. Cross-section view of the parallel plates system. The variation of the capacitance is always negative independently of the movable plates (yellow) going up or down in reference to the fixed plates (orange).</i>	<i>23</i>
<i>Figure 11. Variation of capacity with thinned plates (yellow). When the movable thinned plates move down from the fixed plates (orange) the variation is negative, otherwise, the variation stays zero.</i>	<i>24</i>
<i>Figure 12. The final structure for one "comb" of plates. In orange, it shows the fixed thinned plates, yellow the thinned movable plates and red the fixed non-thinned plates structures.</i>	<i>24</i>
<i>Figure 13. COMSOL model of a single current carrying bar magnetometer.</i>	<i>25</i>
<i>Figure 14. COMSOL eigenfrequency simulation with a single current carrying bar magnetometer. 1) Z-axis movement, 2) Y-axis movement, 3) Z&Y-axis movement and 4) X&Y-axis movement.</i>	<i>26</i>
<i>Figure 15. Simplified (Up) and AutoCAD (Down) version of Magnetometer with 1 current carrying bar.</i>	<i>27</i>
<i>Figure 16. Simplified (Up) and AutoCAD (Down) versions of the magnetometer with 2 current carrying bars with detached parallel plates.</i>	<i>28</i>
<i>Figure 17. Simplified (Up) and AutoCAD (Down) version of Magnetometer with 3 current carrying bars with the detached parallel plates.</i>	<i>29</i>

Figure 18. 3 current carrying bar magnetometer eigenfrequency test. The top image represents the first eigenmode at 4026 Hz with a displacement of mass at Y-axis. The bottom figure represents the second eigenmode at 4976Hz with a displacement of mass in the Z-axis.....	31
Figure 19. Magnetometer adaptation. Before shows the magnetometer with the parallel attached to the outside of the current carrying bars while the after image parallel plates are attached to the inside. ...	33
Figure 20. Simplified (Top) and 3D model (Bottom) view of the magnetometer model that was used in this work.	36
Figure 21. Eigenmode test of the final structure. On the left Z-axis eigenmode at 4976.7Hz and on the right Z&Y-axis eigenmode at 8633.8Hz.....	36
Figure 22.Simplified Silicon Wafer Layers.....	37
Figure 23. Optical lithography process of negative resist. 1) Photoresist deposition. 2) Exposure. 3) Development.	39
Figure 24. Magnetron Sputtering Process. Adapted From [56].	39
Figure 25. GS process with three (Null, medium and maximum) different laser intensities.PR refers to the photoresist layer and Si to the silicon. Adapted from [59].	40
Figure 26. Diagram of PECVD process reactor. Adapted from [61].	41
Figure 27. Schematic of isotropic and anisotropic plasma etching. Taken from [62].	42
Figure 28. Principles of the Bosch Process. Adapted from [65].	43
Figure 29. Magnetometer Fabrication Process. 1) SOI wafer. 2) Metal Deposition and Patterning and SiO ₂ deposition. 3) Frontside Grayscale lithography and SiO ₂ etch. 4) Backside lithography and SiO ₄ Etching. 5) Frontside Silicon Etch. 6) Backside Silicon Etch and structural release.	44
Figure 30. Simplified metal layer processes. 1) Deposition of AlSiCu and PR. 2) PR patterning and development. 3) Metal chemical etching and resist strip.	45
Figure 31. Frontside and backside PECVD SiO ₂ deposition process. 1) starting wafer. 2) SiO ₂ deposition.	45
Figure 32. Simplified frontside grayscale process. 1) Photoresist deposition. 2) Grayscale patterning and photoresist development. 3) SiO ₂ RIE etching. 4) Partial photoresist stripping. 5) SiO ₂ etching. 6) Photoresist removal.	45
Figure 33. Simplified backside SiO ₂ etching. 1) Photoresist deposition. 2) Photoresist patterning and development. 3) SiO ₂ RIE etching.	46
Figure 34. Simplified frontside silicon etching. 1) Initial wafer. 2) Silicon DRIE etching. 3) SiO ₂ RIE Etching. 4) Silicon DRIE etching. 5) SiO ₂ removal and cleaning.	47

<i>Figure 35. Simplified backside etching and release. 1) SOI structure. 2) Silicon DRIE etching. 3) BOX and remaining SiO₂ etching.</i>	<i>47</i>
<i>Figure 36. GS1 mask structure KLayout model.</i>	<i>48</i>
<i>Figure 37. GS1 and GS2 masks KLayout model.</i>	<i>49</i>
<i>Figure 38. GS3 mask structure KLayout model.</i>	<i>49</i>
<i>Figure 39. GS1 and METAL structure KLayout model.</i>	<i>50</i>
<i>Figure 40. TRENCH structure KLayout Model.</i>	<i>50</i>
<i>Figure 41. Complete structure layout.</i>	<i>51</i>
<i>Figure 42. Parallel plate gap testing (left) and calibration (right) devices KLayout models.</i>	<i>51</i>
<i>Figure 43. Single unit layout. All versions of the magnetometer and testing devices were assembled in a single unit so it can be replicated throughout the wafer.....</i>	<i>52</i>
<i>Figure 44. Final wafer layout.....</i>	<i>53</i>
<i>Figure 45. Photoresist deposition and patterning step results by optical microscope</i>	<i>54</i>
<i>Figure 46. Magnetometer pads and lever-like bars after chemical etching by optical microscope.</i>	<i>54</i>
<i>Figure 47. MATLAB constants and parameters.....</i>	<i>63</i>
<i>Figure 48. MATLAB geometrical Parameters.</i>	<i>64</i>
<i>Figure 49. MATLAB electrical and mass parameters.....</i>	<i>65</i>
<i>Figure 50. MATLAB slide damping model.....</i>	<i>65</i>
<i>Figure 51. MATLAB mechanical stiffness models.</i>	<i>65</i>
<i>Figure 52. MATLAB resonance frequency and Q-factor simulations.</i>	<i>66</i>
<i>Figure 53. MATLAB Lorentz force.....</i>	<i>66</i>
<i>Figure 54. MATLAB simulation parameters.</i>	<i>67</i>
<i>Figure 55. Excel sheet of several experiments.</i>	<i>67</i>
<i>Figure 56. Five-step fabrication process runsheet pages.</i>	<i>68</i>

TABLE INDEX

<i>Table 1. Stat of art Lorentz force MEMS magnetometers comparison.</i>	<i>7</i>
<i>Table 2. Comparison between different types of magnetometer technology.</i>	<i>8</i>
<i>Table 3. MEMS Magnetometer objectives.</i>	<i>17</i>
<i>Table 4. Gain experiment between the Lorentz and lever-like bars on a current carrying bar. Gain is given by the percentual decrease in the stiffness from instances 1 to 2. The cross-section of both the Lorentz and Lever-like bars is fixed at 18x25 μm^2 (width x height) and the springs at 5x5 μm^2.</i>	<i>20</i>
<i>Table 5. Parallel plate structure variables following figure 9.</i>	<i>23</i>
<i>Table 6. Correlation between the objective parameters of the device and the structural increase of its properties. Green representing positive effects, red negative, and yellow neutral.</i>	<i>27</i>
<i>Table 7. Two CCBs magnetometer tests in COMSOL and MATLAB with a fixed number of plates and, Lorentz and lever-like sizes. SL, SW and SH represent the length, width and height of the spring.</i>	<i>29</i>
<i>Table 8. Three current carrying bars magnetometer tests with a fixed number of plates and, Lorentz and lever-like sizes. SL, SW and SH represent the length, width and height of the spring.</i>	<i>30</i>
<i>Table 9. An additional test to a three CCB magnetometer where the number of fixed plates was increased to 160.</i>	<i>30</i>
<i>Table 10. Resistance test where CCB represents the current carrying bars and the parallel plates (PP)</i>	<i>32</i>
<i>Table 11. Parallel plate height reduction experiment.</i>	<i>33</i>
<i>Table 12. Main structure tests. LZ-L represents the length of the Lorentz bar and LL-L the length of the lever-like bar.</i>	<i>34</i>
<i>Table 13. Final magnetometer values divided between structural and physical parameters for a 20nT magnetic field at 1mBar pressure.</i>	<i>35</i>
<i>Table 14. ISO cleanroom standards 5 and 6.</i>	<i>38</i>
<i>Table 15. Different device and test structures versions.</i>	<i>52</i>

LIST OF ABBREVIATIONS, INITIALS, AND, ACRONYMS

SQUID – Superconducting Quantum Interface	Q_{pr} – Relative Flowrate Coefficient
Devices	K_n – Knudsen Number
MEMS – Microelectromechanical Systems	m – Meter
INL – Iberian Nanotechnology Laboratory	Ω – Ohm
IC – Integrated Circuits	DL – Damper Length
DOF – Degrees of freedom	D1 – Parallel plate distance
IMU – Inertial Measurement Units	ΔC – Variation of Capacitance
FSR – Full-Scale Range	C0 – Nominal Capacity
Hz – Hertz	PP – Parallel Plates
T – Tesla	SOI – Silicon-on-Insulator
CCB – Current Carrying beam	SiO ₂ – Silicon dioxide
FM – Frequency Modulated	BOX – Sacrificial buried oxide
AM – Amplitude Modulated	ISO – International Organization for
Q – Quality	Standardization
Pa – Pascal	DC – Direct-Current
a – Atto	RF – Radiofrequency
F – Faraday	AlSiCu – Aluminium-Silicon-Copper
μ – Micro	GS – Grayscale
n – Nano	PECVD – Plasma-Enhanced Chemical Vapour
A – Ampere	Deposition
AMR - Anisotropic Magneto Resistance	CVD – Chemical Vapour Deposition
TMR – Tunnel Magnetoresistance	RIE – Reactive Ion Etching
MTJ – Magnetic Tunnel Junction	DRIE – Deep Reactive Ion Etching
GMR – Giant Magnetoresistance	C_4F_8 – Octafluorocyclobutane
p – Pico	SF_6 – Sulphur Hexafluoride
f – Femto	PR – Photoresist
f_0 – Resonance Frequency	DWL – Direct Laser Wright
Δf – Frequency Mismatch	
Q_{eff} – Effective Quality Factor	

1. INTRODUCTION

The understanding and detection of magnetic fields have always been an essential topic to the advancement of science. From this desire to understand its properties, humankind tried to develop devices capable of reading the said fields. From compasses to more advanced magnetic field sensors, humanity has found several areas of application where the reading of magnetic fields has turned advantageous in the pursuit of its objectives in different areas. These areas range from military [1] to medical [2] passing through aerospace [3] and many others. It's in the spatial investigation area that this work has its focus. Even though many technologies surged to read magnetic fields, from giant magnetoresistance magnetometers to superconducting quantum interface devices (SQUID) that present the highest sensitivity on the market, they don't yet allow for high degrees of miniaturization, which brings problems with cost levels and integration in MEMS (**M**icro**E**lectro**M**echanical **S**ystems) sensors. Here is where Lorentz-force-based magnetometers have proven to be a field worth investigating due to their adaptability to MEMS technology and simple understanding.

In this work, a magnetometer capable of reading magnetic fields in the X or Y direction is developed, simulated, and fabricated targeting space applications. The fabrication process is developed at the Iberian Nanotechnology Laboratory (INL) where several high-end manufacturing techniques were studied and integrated into the fabrication of the device.

The specific objectives of the Master thesis leading to this dissertation were the following significant topics:

- Study and development of an introductory literature review of the several areas of MEMS and magnetic field research areas.
- An understanding of the different physical parameters that envelop the design of a magnetometer to be able to calculate the best parameters.
- Learning several simulation tools and drawing programs to simulate and sketch the magnetometer.
- Complementary study of the several fabrication techniques used at INL.
- Fabrication of the MEMS magnetometer.

The present dissertation is organized into six chapters. The first, the Introduction, describes the motivation, objectives, and challenges of this work. The second, MEMS Magnetometry, is an introduction to the MEMS industry followed by the part that the Lorentz-force-based magnetometers take in the magnetometry world as well as complementary information about other types of technology used in the

studying of magnetic fields. Chapter three, Analytical Model, is dedicated to the understanding of the physical formulas that make a magnetometer with a section dedicated to the formulation of the physical objectives that were taken into consideration when developing the magnetometer. Chapter four, Design and Simulations, presents the model and subsequent design problems along with the simulations that were built on the suggested model. Chapter five, Microfabrication, is the theoretical introduction and results of the fabrication steps that were proposed for the manufacture of the magnetometer at INL with a dedicated chapter for the layouts to be used. Finally, chapter six, Conclusion, summarizes the working experience and suggests further topics to be developed in future investigations.

2. MEMS MAGNETOMETRY

2.1 MEMS Technology

MEMS or Microelectromechanical systems are integrated micro devices or systems relating electrical and mechanical components, developed by using Integrated Circuits (IC) compatible with batch-processing techniques [4]. The size of this technology can range from micrometres to millimetres. They include systems capable of sensing, signal processing, actuation, display and control. The capability of integration with electronics (processing and control) on the same surface makes them remarkable systems to work with.

From the development of MEMS Technology came the design and production of revolutionary sensors (devices capable of converting physical or chemical quantities into something perceptible) and actuators (transform energy to produce action). Several methodologies are used ranging from electrostatic and magnetic to thermal and piezoelectric actuation. Both sensors and actuators are referred to as transducers [5].

This technology involves a broad scope of domains to measure information from the surrounding environment and convert it into electrical signals. These domains are [5]:

1. Electrical (Electric field, current, voltage, resistance, etc).
2. Chemical (Composition, reaction rate, concentration, pH, etc).
3. Mechanical (Length, area, width, velocity, acceleration, force, etc).
4. Thermal (Temperature, flow, heat, entropy, etc).
5. Radiative (Intensity, phase, polarization, wavelength, etc).
6. Magnetic (Field intensity, permeability, flux density and magnetic moment).

This has led to the wide-ranging adaptation of MEMS devices to diverse fields of application like biomedical [6], industrial [7], automotive [8], etc [9]. Another factor that allowed the spread of MEMS devices was the ability to introduce batch fabrication processes, by the microelectronics industry, which allowed for a low-cost method to mass produce large quantities of identical devices [10].

2.1.1 MEMS magnetometers

Nonetheless, the research in this field is still very active with many advantages when compared with the already existing technologies, the majority of these being directly related to MEMS technology itself, which is already one of the leading ones for accelerometers [11] and gyroscopes [12] in the consumer goods field. Some of the advantages are:

- Multi-Degrees-of-freedom (DOF) Inertial Measurement Units (IMUs) can be fabricated in a single chip [13], leading to area and subsequent cost savings.
- Nearly perfect alignment with accelerometers and gyroscopes axes (Due to the fabrication occurring on the same chip). This avoids problems with alignment and calibration which are typical of multi-DOF hybrid IMUs. Better precision of the measurement is achieved as it also depends on the misalignment between different sensors [14].
- The use of a magnetic flux concentrator is not needed. They are mostly used in AMR, GMR, TMR, and Hall sensors to change the direction of the external field [15] or to mitigate the $1/f$ noise [16]. This avoids problems that may arise from the thinning trend of packages.
- Flexible operation range and the sensing of a magnetic field in all three axes can be achieved with planar structures. This is uncommon in other technologies.

Throughout the years, different approaches to the development of MEMS magnetometers were tested, some of them with interesting results, one of them being MEMS magnetometers with deposition of magnetic materials on top of the silicon structure [17]. They exploit the interaction between the ferromagnetic material and the external magnetic field to create a torque on the structure.

MEMS magnetometers based on the *Lorentz-Force principle* have been the subject of study in these last years and they will be further discussed as they are the subject of this dissertation.

2.2 Lorentz force MEMS Magnetometers

MEMS magnetometers based on Lorentz force exploit the properties of the interaction between a current-carrying beam (CCB) and a magnetic field that'll cause a movement of that beam (and the attached suspended mass). This force is commonly measured using one of two modulation approaches. The first one is a frequency-modulated (FM) device where the device is realized by using the Lorentz force to create either a shift in the resonance frequency [18] or the oscillation frequency (also known as quadrature frequency modulation operation) [19]. The second one is an amplitude-modulated (AM) device where a variation in the amplitude of the displacement caused by a force is used to read the magnetic field. In this work, an AM approach is used. This has several advantages such as:

- Magnetic field proportional to the displacement and direct capacitance transduction – capacitive readout circuits, can be used.
- The ability to operate the device at its resonance frequency. This translates to a higher gain on displacement.
- The operation at resonance frequency is usually at kHz or higher. This lowers the impact of the $1/f$ noise [20].

Operation at resonance frequency implies that for the same external field, and thus the same Lorentz force, the displacement of a resonance-operated device is greater than a quasi-static (near DC) one by a factor, normally, higher than one. This can then be sensed, most commonly, in either a capacitive, piezoresistive [21] or optical readout [22].

This approach also has some disadvantages such as:

- High electrical resistance when using springs increases the compliance of the CCBs to enhance the displacement.
- A trade-off between sensitivity and bandwidth [23].

2.2.1 State of art

Most research done in the Lorentz force MEMS magnetometer area uses the Quality-factor (Q-factor) amplification at resonance operation to boost the displacement. This takes in certain physical properties of the device that are modelled to increase the Q-factor to its maximum level possible.

An interesting device was designed by Xiaoxiao Song et al. [24] where a MEMS resonant Lorentz-force magnetometer was conceived for having a max Q-factor enhancement with the encasement for the device

at near-vacuum pressure. They were able to achieve a 70120 Q-factor at 1 Pascal (Pa), which is the highest found for this type of device, using a magnetometer that features a structural topology to minimize thermoelastic dissipation. They also employ an energy injection technique based on parametric pumping to further improve the Q-factor.

Continuing the talk about Q-factor amplification, Varun Kumar et al [25] were able to develop an amplitude-modulated Lorentz force MEMS magnetometer with pico-tesla sensitivity by artificially boosting the effective quality of the resonator through the modulation of the bias current. They were able to achieve an increase from 680 to 1.1×10^6 on the Q-factor by tuning the bias current although it suffers from low bandwidth.

Another interesting magnetometer, from the layout perspective, is a dual-axis magnetometer developed by Aditi et al. [26] adapted from a two-DOF torsional gyroscope structure. In this magnetometer, two different frequencies of operation are referred to detect fields in the X and Y direction where if the magnetometer is operating at 107kHz the device would read fields in the X plane and 187kHz for fields in the Y plane. The only problem is that the Q-factor is on the lower side of the spectrum (8 for the Y-axis and 2 for the X-axis). An off-resonance approach to increase the bandwidth of a magnetometer was developed by Langfelder et al [27] through the use of a slightly lower operation frequency when compared to the mechanical resonance frequency, and a 0.25 mbar packaging. In this work, two magnetometers were compared where the magnetometer operated off-resonance had a four times larger bandwidth. Finally, the basis of this work is a magnetometer developed by Rosana Dias et al. [28] capable of reading magnetic fields in the Z-plane with geometrical improvements to increase the displacement resulting from Lorentz forces. It uses a combination of multiple Lorentz force generating bars and off-resonance operation to achieve a sensitivity of 50.5 atto-Faraday per micro-Tesla (aF/ μ T) variation or 1aF when a 20 nano-Tesla (nT) magnetic field is present which will be used as the baseline of this dissertation. All this while maintaining a low impedance, a $2.65 \text{ nT}/\sqrt{\text{Hz}}$ thermomechanical noise and a 50Hz Bandwidth operating at 4 milliamperes (mA) per bar and a 1mBar vacuum. Table 1 shows a comparison between the above-referenced magnetometers.

Table 1. Stat of art Lorentz force MEMS magnetometers comparison.

Sensor	Q-factor	Current [mA]	Bandwidth [Hz]	Sensitivity
Xiaoxiao Song et al [24]	70120	4.2	2.95	$0.55 \text{ Hz} \cdot \text{nN}^{-1}$
Varun Kumar et al [25]	1.1×10^6	7.245	0.34	$2.107 \text{ mV} \cdot \text{nT}^{-1}$
Langfelder et al [27]	668	0.05	200	$72 \text{ mV} \cdot \text{mT}^{-1}$
Rosana Dias et al. [28]	240	4	50	$102 \mu\text{V} \cdot \mu\text{T}^{-1}$

2.3 Technology comparison

The diversity of areas of application of magnetic field sensing has led to the development of diverse types of sensing technologies [29] capable of reading a wide variety of magnetic field ranges as seen in figure 1 where we can find a multitude of technologies applied in magnetometers with their respective magnetic field range.

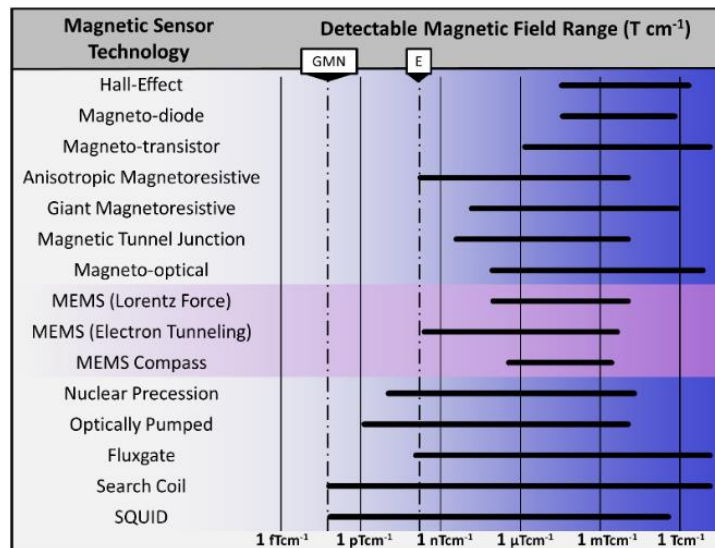


Figure 1. Comparison between different kinds of magnetic sensor technology. Adapted from [30].

Some of the most diffused technologies used in commercial products are:

- *AMR (Anisotropic MagnetoResistance)* – a phenomenon that occurs in ferromagnets in which the resistivity depends on the angle between the current and magnetization directions [31]. They get a good resolution but have a limited range and need a set-reset procedure (increases power consumption). The dependence on ferromagnetic materials also carries some problems with hysteresis and magnetic domain flipping.
- *TMR (Tunnel MagnetoResistance)* – a magnetoresistive effect that occurs in an MTJ (Magnetic tunnel junction). When two ferromagnets are separated by a thin insulator, electrons can *tunnel* from one ferromagnet to another. These magnetometers present an excellent resolution but have a complex fabrication method, high-temperature dependence, high offset and can be damaged by high magnetic fields [32].
- *GMR (Giant MagnetoResistance)* – sensors that change their electrical resistance in response to fluctuations in the magnetic field [33]. They present some of the best resolutions in the market but have some drawbacks such as nonlinearity, hysteresis, offset, and a temperature-dependent output that can compromise the measurement accuracy. In addition, some GMR sensors have a unipolar output which limits their applications in AC measurements [34].
- *Hall Effect* – a current is applied to a thin sheet of metal. In the presence of a magnetic field perpendicular to the direction of the current, the charge carriers are deflected by the Lorentz force, producing a difference in electrical potential between the two sides of the strip proportional to the strength of the field [35].
- *SQUID (superconducting quantum interference device)* – consists of a macroscopic superconducting loop with one or two weak links (Josephson Junctions). These are the world's most sensitive sensors. They incur some problems such as a very low temperature of operation, can't be subjected to large currents and the fabrication process is extremely complex [36].

In table 2 some examples of the different types of working principles are shown as listed above:

Table 2. Comparison between different types of magnetometer technology.

Sensing Principle	Current [mA]	BW [Hz]	Resolution
AMR[37]	-	-	150 [nT/√Hz]

MTJ[2]	-	-	200 [pT/\sqrt{Hz}]
GMR[38]	3	-	125 [pT/\sqrt{Hz}]
Hall Effect[35]	70	10	5 [pT/\sqrt{Hz}]
SQUID[39]	0.045	-	3.5 [fT/\sqrt{Hz}]

3. ANALYTICAL MODEL

In this chapter, an explanation of the most important physical properties will be contextualized to be able to create an analytical model that's used to determine the best parameters for a Lorentz-force-based magnetometer.

3.1 Lorentz Force

Figure 2 shows an example of the application of a current (i) on a CCB in the presence of an external magnetic field (B). This interaction will result in an upward force (-z-direction). Said force is called the Lorentz force and it not only depends on the intensity of the current and magnetic field but also on the length (L) and number of CCBs (N_{CCBs}).

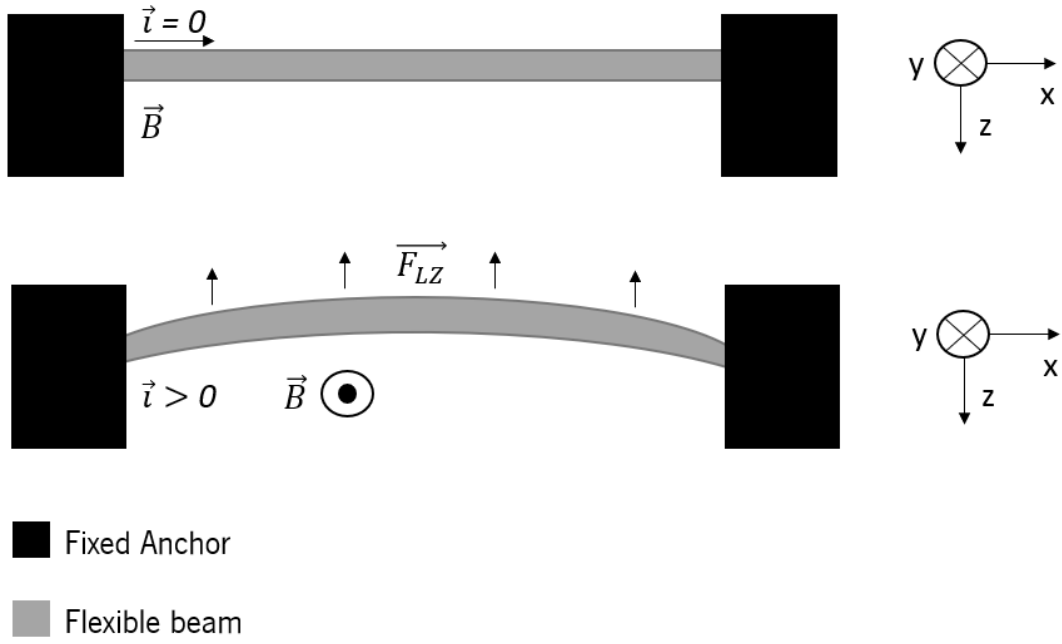


Figure 2. Before (Top) and after (Bottom) a current is applied to the CCB.

The formula of the force can be written as [40]:

$$F_{LZ} = N_{CCBS} \cdot i \cdot L \times B \text{ [N]} \quad (3.1)$$

This force causes a displacement (x) of the bar from its resting position given by:

$$x = \frac{F_{LZ}}{k} \text{ [m]} \quad (3.2)$$

Where k is the mechanical stiffness coefficient of the bar.

This property can be used on a capacity sensing technology where the displacement of the body will result in a variation of the electrical capacitance of the device. Being able to read this variation can then be used to determine the intensity of the magnetic field.

A problem that arises when dealing with Lorentz-Force-based magnetometers is the force itself. When considering typical MEMS devices, the force generated from a conventional magnetic field turns out to be around two orders of magnitude lower than Coriolis forces obtained in a gyroscope, and three orders of magnitude lower than the inertia one in a regular accelerometer. This has a direct effect on the displacement of the mass in the Lorentz bar affecting the measured capacitance variation (the lower the displacement the lower the variation).

3.2 Capacitive Readout

For the detection of the intensity of the magnetic field, the device from this work relies on the variation of the capacitance (C) when a displacement (Δx) occurs. This is achieved through the capacitance variation between electrodes with plates or beam shapes. They provide fixed and moving electrodes that are relatively straightforward to fabricate. This implies that the displacement is capacitively transduced into an electrical signal. In figure 3 an example of the capacitance detection method used is shown where fixed plates (orange) are placed at the distance of d_1 from movable plates (yellow). On the left side, plates in their stationary state can be found and, when the capacitance is measured the nominal capacitance (C_0) is attained. When a displacement is applied to the movable plates there will be a variation in the capacity of the device due to the reduction of the overlapping area of the plates (C_x).

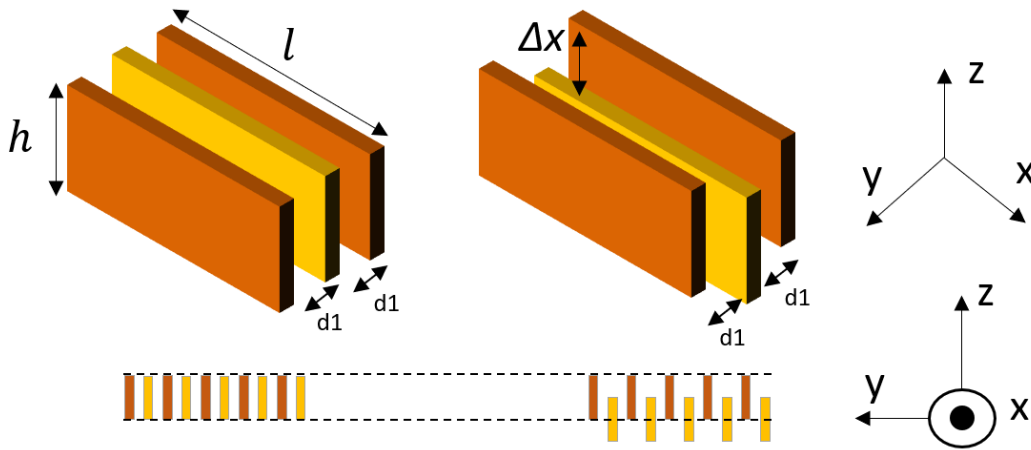


Figure 3. Displacement of plates before (left) and after (right) a force is applied.

The theoretical capacitance variation can be obtained through the following equations[5]:

$$C = \epsilon_0 \frac{h \cdot l}{d_1} [F]$$

$$\Delta C = C_0 - C_x = \epsilon_0 \frac{(h - |\Delta x|)l}{d_1} = C_0 - \epsilon_0 \frac{|\Delta x|l}{d_1} [F] \quad (3.3)$$

Where h and l are, respectively, the height and length of the plates and ϵ_0 is the dielectric constant of the medium (air in this case). From the formula above it's determined that the initial height of the capacitor plate doesn't intervene in the variation of the capacitance. This will be important at a later stage.

3.3 Increasing the Lorentz Force

As explained at the end of chapter 3.1, in itself, the Lorentz Force requires a slight boost to achieve a higher displacement. A direct way to achieve this would be to increase the current supplied to the device

since, by the formula (3.1), it would lead to a direct increase in force, but it would also cause a direct increase in power consumption.

When talking about MEMS devices, these are modelled as second-order spring-mass-damper [41], which means that their force-to-displacement transfer function is not constant in frequency. According to figure 4 at around 1.46×10^4 Hz the amplitude of the vibration is much higher than the one at 1.4×10^4 Hz. This happens due to the mechanical resonance frequency (f_0) in a structure. When an excitation occurs at f_0 it will amplify the displacement by a quantity dependent on the quality factor (Q).

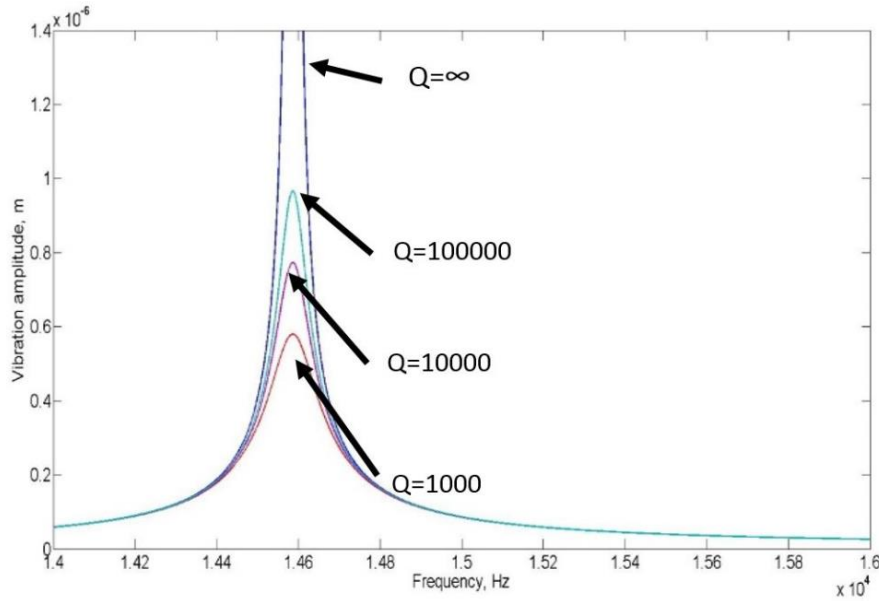


Figure 4. Vibration amplitude vs Frequency due to various quality factors, taken from [42].

If formula (3.2) is taken into consideration and the quality factor is multiplied, at an excitation frequency equal to the mechanical resonance frequency, the following formula is obtained:

$$x_{f=f_0} = \frac{Q \cdot F_{LZ}}{k} [m] \quad (3.4)$$

In a MEMS magnetometer, this can be achieved by injecting a driving current at the structure resonance frequency [28]. This way the displacement would be further increased by a factor dependent on the characteristics of the designed structure.

From formula (3.4) it's shown that the introduction of the quality factor gives considerable help regarding the Lorentz force problem, but it also has some drawbacks:

- Bandwidth/Q factor trade-off: The bandwidth of a system is calculated through the formula[43]:

$$BW = \frac{f_0}{Q} [Hz] \quad (3.5)$$

So, when the Q factor is increased to enhance the displacement of the device, there will be a direct negative impact on the bandwidth.

- Current Generation: Maintaining the current oscillating at the same level as the natural frequency of the device is not a trivial matter. The assistance of an oscillator circuit is required.
- In AM devices with parallel-plate-based readout, when the number of plates increases so does the output electrical signal increase, but it takes a negative toll on the bandwidth. It also has a direct correlation with the increase in the damping which is shown in section 3.5.

3.4 Bandwidth

As given by formula (3.5) bandwidth is the frequency range in which the magnetometer operates. It characterizes how well a magnetometer tracks rapid changes in the magnetic field. A higher bandwidth allows a magnetometer to faithfully reproduce a rapidly fluctuating actual field. This is important when mapping out magnetic anomalies as the measurement bandwidth should be high enough not to distort those anomalies [44]. Practically, the bandwidth of a mechanical device is the frequency range when the amplitude of the signal has a drop-off of -3dB around its resonance frequency.

According to [45] the resonance frequency (f_0) and the quality factor (Q) are, respectively, given by:

$$f_0 = \frac{1}{2\pi} * \sqrt{\frac{k}{m}} [Hz] \quad (3.6)$$

$$Q = \frac{2\pi \cdot f_0 \cdot m}{b} \quad (3.7)$$

Where m is the effective mass of the device and b is the damping coefficient. If we take these formulas and add them to (3.5) we can determine that the bandwidth is given by:

$$BW = \frac{b}{2\pi m} [Hz] \quad (3.8)$$

One of the objectives of the magnetometer is to achieve a minimum bandwidth of 50Hz.

If a resonance frequency (f_0) of 5000Hz and a Q factor of 1000 is adopted, which is similar to the output of this work, by formula (3.5), the device will have a bandwidth of 5Hz. This is an extremely substandard result, and something must be done to increase the bandwidth.

3.4.1 Off-Resonance Operation

As seen in work [27], operating at a frequency with a slight variation from the resonance frequency will increase the bandwidth of the device and thus reduction of the Q factor. This is a trade-off between a higher displacement or higher bandwidth as shown in figure 5 where, depending on the deviation from the resonance frequency, the Q factor will decrease the more it steps away from f_0 .

This technique is called *off-resonance* or *mode-split operation*. It's defined as the operation of a sensor with an excitation frequency slightly different (f_d) from the mechanical resonance [27]. This mismatch is defined as:

$$\Delta f = |f_0 - f_d| [\text{Hz}] \quad (3.9)$$

Figure 5 reveals the difference between the Q factor of a high and low damping coefficient which goes in conformity with the formula (3.8) where a high damping coefficient runs along with higher bandwidth and a lower Q and vice-versa. As the frequency of operation strays away from f_0 (f_s if we look at figure 5) the bandwidth increases in accordance with Δf .

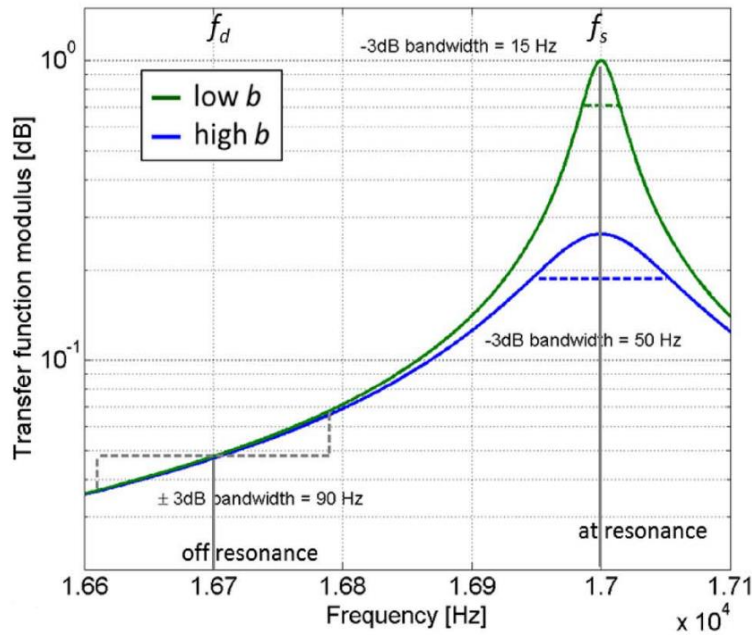


Figure 5. Bandwidth comparison between resonance and off-resonance operation for two different devices o the first one with a Q of 600 and the second with a Q of 150. Taken from [27].

In conclusion, if we inject a driving current with a frequency mismatch Δf for f_0 an increase in the bandwidth of the device is obtained at the cost of the quality factor. This new quality factor is denominated in this work as the *effective quality factor* (Q_{eff}) that's highly dependent on Δf .

3.5 Damping Coefficient

MEMS devices are usually surrounded by a gas, most of the time its air, and when they move or vibrate, they interact with said gas. This results in damping, spring and inertial forces acting on the vibrating structure which may be important to the operation of the MEMS device. Out of these three, the most dominating at low frequencies is the damping force. The damping in MEMS structures is dominated by their small characteristic dimensions which leads to the following observations[46]:

- The damping force is dominated by the viscosity.
- The rarefied gas effects are present, especially at pressures below the ambient pressure.
- The amplitude of the oscillation is large compared with the dimensions of gas volumes.

For this work, viscosity-dominated flow in narrow air gaps is assumed. This is the assumption that incompressible and inertialess flow is made. In this case, the damping force does not depend on the frequency and is relative to the viscosity coefficient, μ . This coefficient depends on temperature, T_0 , but not on pressure. It's given by:

$$\mu = \mu_R \cdot \frac{T_R + C}{T_0 + C} \left(\frac{T_0}{T_R} \right)^{\frac{3}{2}} \left[\frac{N \cdot s}{m^2} \right] \quad (3.10)$$

where C is the Sutherland constant, and μ_R is the viscosity at temperature T_R . These values can be found in the case of air where $\mu_R = 18.45 \cdot 10^{-6} \left[\frac{N \cdot s}{m^2} \right]$, $T_R = 308K$ and $C = 112K$ [47].

3.5.1 Slide Damping

Figure 6 shows the slide damper geometry where the body moves (oscillates) tangentially with the surface. This can typically be found in surface micromachined structures, under the moving mass and between the fingers of comb-drives such as in the case of this work. The gas motion is excited by the force on the surface of the moving body. The damping force is also caused by the friction between the viscous gas and moving layers. As there will be no considerable pressure variation across the surface of the damper we can assume the damping force is constant over its surface[46].

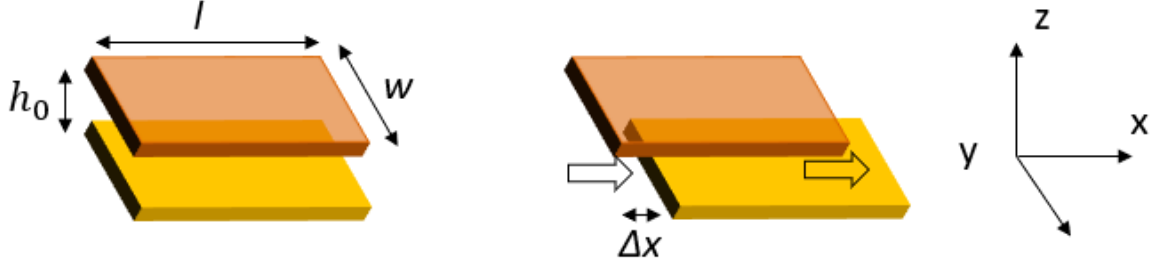


Figure 6. Topology of a slide damper (left). The surface moves tangentially to the surface (right).

The damping coefficient can be obtained through the subsequent formula[46]:

$$|b| = \frac{\mu \cdot A}{Q_{pr} \cdot h_0} [N \cdot s/m] \quad (3.11)$$

Where A is the area of the damper, h_0 is the distance between the plates and Q_{pr} is the relative flow rate coefficient. Q_{pr} is a function of the Knudsen number (K_n) that represents the mean free path of the gas (λ) divided by the air gap height (h), $K_n = \lambda/h$ [46]. From Veijola et al. [48] a Q_{pr} approximation is obtained:

$$Q_{pr} = 1 + 2K_n + 0,2K_n^{0.788} \cdot e^{-K_n/10} \quad (3.12)$$

This mathematical approximation has an accuracy of $\pm 0.6\%$ when it comes to the representation of Q_{pr} in slide-damping models. The model that's utilized by Veijola et al. also suggests that the air gap should be modified by:

$$h'_o = \frac{h_0}{1 + 8.5 \cdot \frac{h_0}{a}} [m] \quad (3.13)$$

Where a is the length of the damper surface. This happens due to the elongation seemingly increasing the resistance at the low-frequency regime only. In this work, there's also a $1,016 \cdot K_n$ correction factor applied to the K_n .

The total damping of a system depends on the number of dampers ($N_{dampers}$) in a system:

$$b_{system} = b * N_{dampers} [N \cdot s/m] \quad (3.14)$$

3.6 Thermo-mechanical noise

A significant source of mechanical loss, in the presence of a sensor, is likely to be the interaction of frictional forces between certain interfaces. Reducing these mechanical losses is expected to yield a higher mechanical Q and a lower thermal-mechanical loss. The thermal-mechanical loss, or input-referred thermo-mechanical noise, can be calculated through the following formula:

$$Nb = \sqrt{4 \cdot K_B \cdot T \cdot b} \times (N_{ccb} \cdot l \cdot i)^{-1} [T/\sqrt{Hz}] \quad (3.15)$$

Where K_B is the Boltzman constant, T is the temperature, N_{ccb} is the number CCBs and l is the total length of the beam.

3.7 Magnetometer target specifications

Before advancing to the design of the device, some objectives must be defined. As referenced before, this work is based on the work developed by Rosana Dias et al. [28] where a Z-axis MEMS magnetometer was designed to meet predefined target specifications. With that in mind, in table 3, certain parameters were stipulated:

Table 3. MEMS Magnetometer objectives.

Parameter	Value
Capacitance Variation for 20nT	$\geq 1aF = 50.5aF/\mu T$
Bandwidth, BW	$\geq 50Hz$
Thermomechanical Noise, Nb	$\leq 3nT/\sqrt{Hz}$
Current carrying bar Resistance, R	$\leq 150\Omega$ per bar
Frequency of operation, $f_{operation}$	$= 4952Hz$
Current, I	$= 4mA$ per bar
Pressure, P	$= 1mBar$

With the parameters in mind, the final objective of this work is to design, simulate and develop a MEMS magnetometer based on Lorentz force with the ability to read magnetic fields in the X and Y directions complementary to the Z-axis magnetometer in [28] (hence the 4952Hz operation frequency). The assembly of these objectives were deemed required for a low-cost capacitive magnetometer for space applications.

The target specifications in table 3 were possible to be accomplished in [27] using an in-plane moving microstructure and through the combination of design and operation improvements, namely: 1-lever-like springs, 2-coupled multiple current-carrying bars, and 3- off-resonance operation. One objective of this work is also to verify if the implementation of those design innovations is possible and results in similar magnitude performance improvement.

4. DESIGN AND SIMULATION

In this chapter, the workflow, as well as the following designs and simulations, will be discussed.

4.1 Simulation Tools

To simulate the properties of the device with the utmost precision there were three main tools used:

- AutoCAD - 3D modelling of the structures.
- COMSOL – Stationary simulation of the structure to obtain the stiffness and modal simulation to obtain eigenfrequencies (natural frequencies at which a system is prone to vibrate[49]) of the structure.
- MATLAB – Computation of other physical properties and performance parameters of the device.

Using these tools, a workflow was created where the device was modelled in AutoCAD then the file would be imported to COMSOL to determine the parameters referenced above and then all the different aspects of the device and the properties simulated in COMSOL would be introduced to MATLAB where the final results of the structure would be calculated. The results would finally be exported to an EXCEL file where each simulation would be compared.

4.2 Current Carrying bar

In the magnetometer, the CCB serves as the most flexible structure of this device. Figure 7 represents a model of a single current carrying bar. These have 3 subsections. In blue, the Lorentz bar is responsible for holding the movable parallel plates. Because one of the objectives is to achieve the highest displacement possible to increase the capacitance variance from a certain magnetic field, other structures were introduced to increase the displacement of this section when compared to a normal straight bar (ex: figure 2). Represented in red, the springs, are thinned-down sections that dominate the reduction of the overall stiffness of the structure. According to formula (3.2) the lower the stiffness the higher the displacement, with special caution that the reduction of the stiffness also negatively impacts the Q factor. Finally, in green, the lever-like structures, are designed to increase the elongation of the Lorentz bar increasing the displacement. An exact mathematical model of the stiffness of the complete structure was attempted, but simplifications lead to an inaccurate model. So, to determine the overall stiffness and resonance frequency of the structure, it was opted to use FEM simulations. The tool that was used to proceed with the simulations was COMSOL.

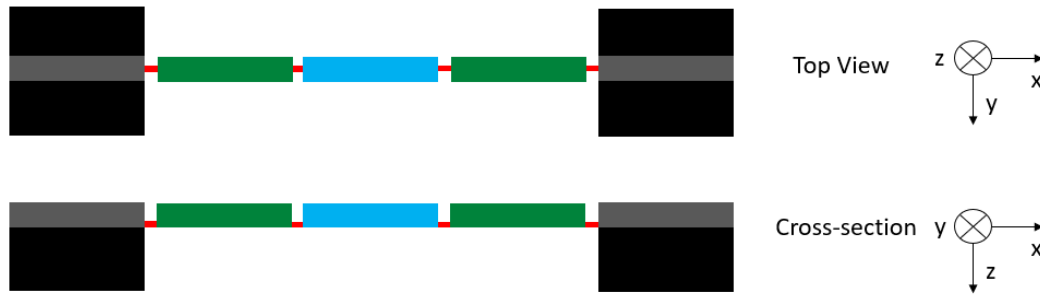


Figure 7. Simple illustration of a single CCB. It has 3 main components, the Lorentz bar (Blue), the lever-like bars (green) and the springs (red).

In order to preserve some of the variables related to this structure, the size of both the Lever-like and Lorentz bars will be the first to be determined. In table 4 some experiments are displayed, completed in COMSOL, concerning the connection between the Lever-like and Lorentz bars. In this experiment, a correlation between both bar sizes was investigated. In the initial setup, one CCB was designed, where its format was spring-lever-spring-Lorentz-spring-lever-spring, and the sum of both Lever-like and Lorentz bars was specified to give $4000\mu\text{m}$. From these tests, it was demonstrated that as the Lorentz bar was decreased and the Lever-like bar increased, the stiffness of the current carrying bar diminished substantially and, when the length of the spring was increased, the stiffness was more efficiently reduced the smaller the Lorentz bar. It's then safe to say that the lower the relation between the Lorentz and Lever-like bars the more efficient it is to adjust the spring to any changes in the whole magnetometer structure.

Table 4. Gain experiment between the Lorentz and lever-like bars on a current carrying bar. Gain is given by the percentual decrease in the stiffness from instances 1 to 2. The cross-section of both the Lorentz and Lever-like bars is fixed at $18 \times 25 \mu\text{m}^2$ (width x height) and the springs at $5 \times 5 \mu\text{m}^2$.

Structures (length μm)				Stiffness (N/m)		
spring-lever-spring-Lorentz-spring-lever-spring						
Lorentz-Bar	Lever-Like Bar	Spring1	Spring2	Stifness1	Stifness2	Gain
2000	1000	15	25	2.3975	1.5445	35.6%
1000	1500	15	25	1.3956	0.8927	36.1%
500	1750	15	25	1.1606	0.7285	37.2%

The final design of the magnetometer had a 500μm Lorentz bar and a 1750μm Lever-like bar length. From here on any adjustments made to the structure were mostly handled in the springs. These mainly served as compensators for the alteration of other parameters and will be further discussed at a later stage.

4.2.1 Electrical resistance

As current will be flowing through these sections, a thin layer of metal was deposited on top of the Lorentz and lever-like structures to reduce the electrical resistance. Due to fabrication issues, a layer of metal above the springs isn't possible which results in a great part of the electrical resistance being concentrated on the springs. One of the main objectives of this work was to achieve an electrical resistance per current path lower than 150Ω. The formula for the resistance of a bar is given by [50]:

$$R_{bar} = \frac{length}{height \times width} \cdot \rho_{material} [\Omega] (3.16)$$

Where ρ is the resistivity of the material of the bar.

The total resistance of one current carrying bar is given by:

$$R_{total} = R_{Lorentz-bar} + 2 \cdot R_{Lever-like} + 4 \cdot R_{Spring} [\Omega] (3.17)$$

Where each R represents the electrical resistance of each subsection of the current carrying bar.

The magnetometer was developed in a silicon wafer which has a resistivity of $1.5 \times 10^{-4} [\Omega \cdot m]$. The metal used to cover the bars has a similar resistivity to the aluminium used in the simulations, which is around $2.82 \times 10^{-8} [\Omega \cdot m]$. This means that the electrical resistance coming from the springs has a factor of 10000 when compared to the other structures. This is something that must be taken into serious consideration when designing the size of the springs.

4.3 Parallel Plates

The parallel plates system is the magnetic field detection method used on the device presented in this work. Figure 8 shows a simplified model of this structure. The movable plates (yellow) are attached to the CCBs and, upon exertion of directional force, generated by a magnetic field (formula (3.1)), the movable plates will move in the same direction of said force. This will create a displacement depending on the strength of the magnetic field. The variation of the overlapping area between the fixed plates (orange) and the movable plates will generate a variation of the capacity given by (3.3). In sum, by taking the initial capacity of the device and capturing the variation of the capacitance (ΔC) when a magnetic field is applied, we can determine the strength of the field by the difference between the two instances. The ΔC is detected by contacts adjacent to the combs of the fixed plates as shown in the figure:

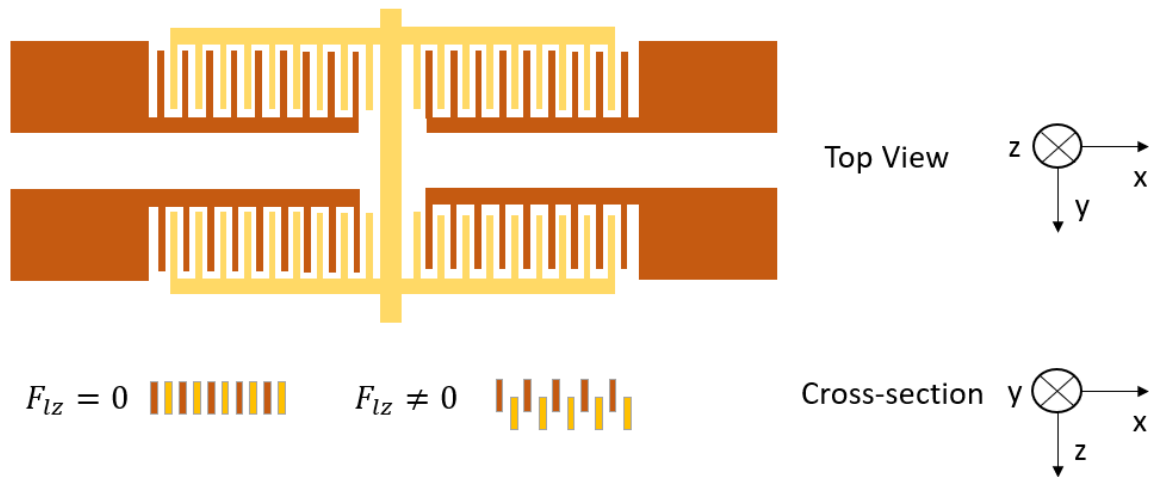


Figure 8. Top view and cross-section of Parallel plates system. Movable parallel plates (yellow) and fixed plates (orange). The cross-section shows the result of a downward Lorentz force.

Figure 9 shows the design of the intercalated fingers in the parallel plates section of the device. For the measurement of the capacity variation, the damper length (DL) is one of the most important variables since it represents the area overlap of a capacitor. The parallel plate distance (d_1) is also important when taking into consideration formula (3.3) since it directly affects the capacity of the device. DL directly correlates to l and D_1 is the same d_1 from the formula.

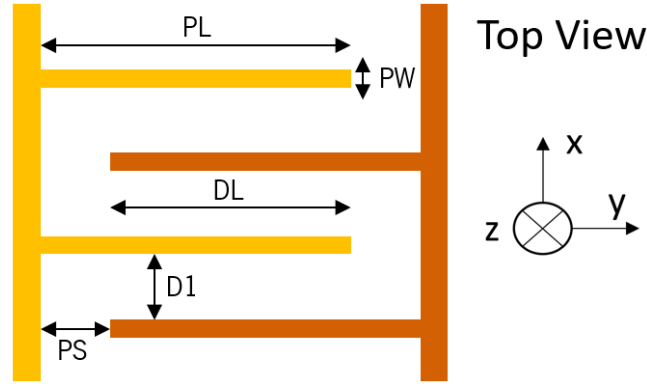


Figure 9. Capacitor parallel plate structure where movable (yellow) and parallel (orange) plates variables are represented. In this structure, the plate length (PL), plate width (PW), damper length (DL), parallel plate distance (D1) and plate separation (PS) variables are shown.

Since the main objective of the parallel plates is to achieve the desired ΔC the design of this structure was formulated with that objective. This considers that the damper length has to be the biggest possible and the parallel plate distance the minimum achievable. In table 5 the values used in the device from this work are displayed:

Table 5. Parallel plate structure variables following figure 9.

Parameters	Value (μm)
Plate length - PL	400
Plate width - PW	7
Damper Length - DL	380
Parallel plate Distance - D1	2
Plate Separation - PS	20

Here a problem is encountered. If the movable plates and the fixed plates have the same size it will be impossible to distinguish if the plates are moving up or down as shown in figure 10. This happens due to, independently of the direction of the force, the overlapping area decreasing, leading to a negative ΔC . This can have problems at a later stage when mapping the direction of the magnetic field.

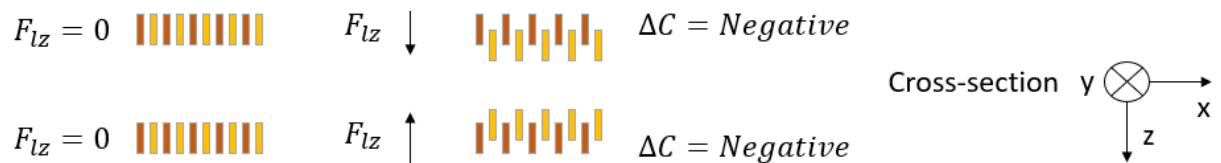


Figure 10. Cross-section view of the parallel plates system. The variation of the capacitance is always negative independently of the movable plates (yellow) going up or down in reference to the fixed plates (orange).

4.3.1 Plate Thinning

To prevent the problem mentioned in section 4.3, there will be a thinning applied to the parallel plates except for a few remnant fixed plates, this has the bonus of vastly reducing the overall weight and damping of the device. This will allow for a differentiation of whether the movable plates are going up or down. With the help of figure 11, it's indicated that when the movable plates go up the ΔC is zero due to the overlapping not changing. On the contrary, when the plates move down the ΔC is negative since the overlapping area decreases.

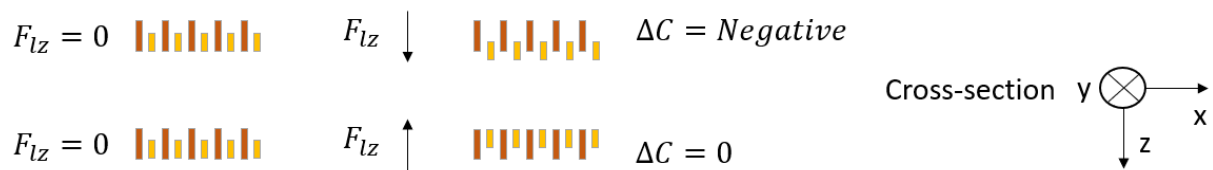


Figure 11. Variation of capacity with thinned plates (yellow). When the movable thinned plates move down from the fixed plates (orange) the variation is negative, otherwise, the variation stays zero.

From here all that's left to do is have separated contacts for non-thinned plates and thinned plates and the problem of not being able to distinguish up from down on the device is solved. Figure 12 demonstrates the final design that was later applied.

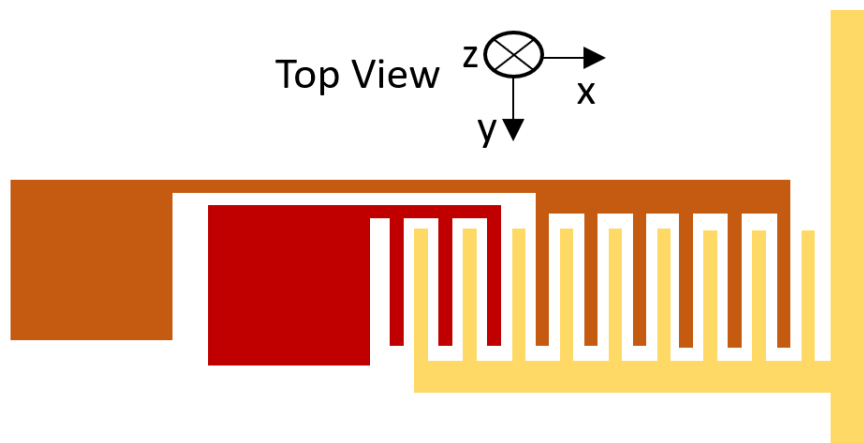


Figure 12. The final structure for one "comb" of plates. In orange, it shows the fixed thinned plates, yellow the thinned movable plates and red the fixed non-thinned plates structures.

4.4 Eigenmode

An eigenmode is a natural vibration of a system such that various parts all move together at the same frequency. The different parts all move sinusoidally at the same frequency and their amplitudes all increase or decrease in proportion to one another. The frequency of a single mode is called an eigenfrequency [49]. The study of these natural frequencies is mostly important to determine the frequency at which a current must be injected into the system for it to move in a certain direction with increased gain. This brings certain problems such as if a natural frequency that allows the structure to move in the X plane with increased gain and a similar frequency that eases the movement in the Y plane when injecting the current at the X plane frequency, interferences will occur in the Y direction because both frequencies are close to each other. This is important when designing the device to minimize movements of the device in directions it isn't supposed to go.

The method of determining these frequencies is through FEM (Finite Element Modelling) simulations such as in COMSOL. First, a 3D model of the structure is drawn in AutoCAD 3D. Then, that model is imported to COMSOL where, in a Solid mechanics interface, an eigenfrequency study is conducted. From here several frequencies are obtained each with its directional mass displacement. Figure 13 shows a model of a single Lorentz bar model used in a COMSOL simulation.

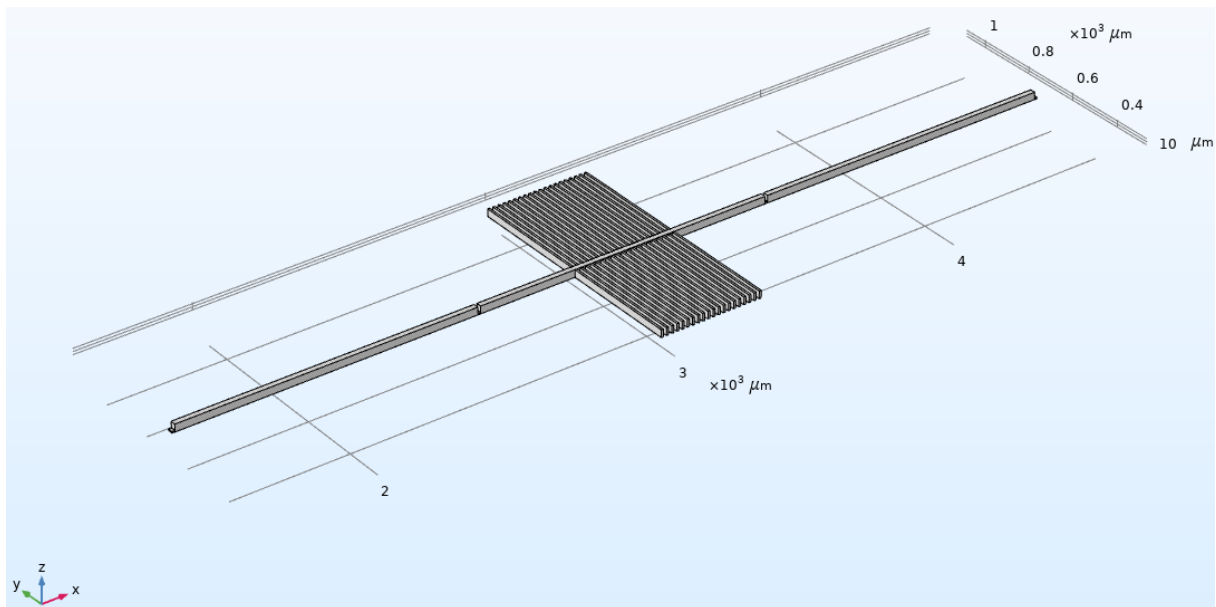


Figure 13. COMSOL model of a single current carrying bar magnetometer.

If an eigenfrequency study is applied to the magnetometer referenced above, as a result, COMSOL will show several frequencies that can then be plotted to see the direction in which they vibrate. A test run was tried for this magnetometer and the results can be seen in figure 14.

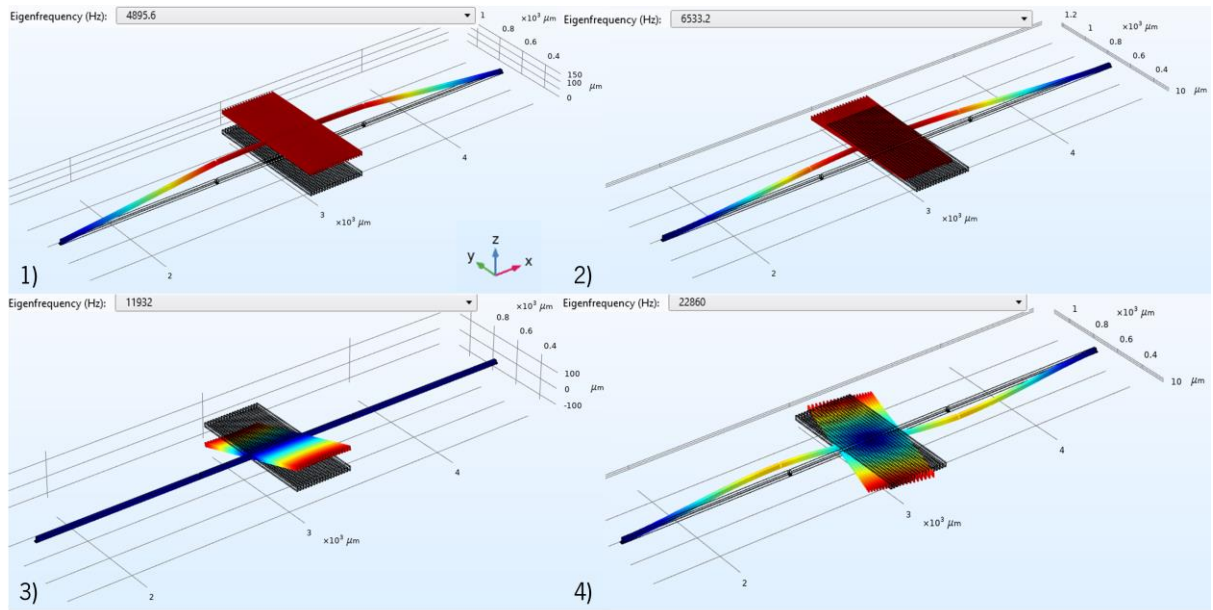


Figure 14. COMSOL eigenfrequency simulation with a single current carrying bar magnetometer. 1) Z-axis movement, 2) Y-axis movement, 3) Z&Y-axis movement and 4) X&Y-axis movement.

In this run, four different eigenmodes were determined:

- Z-axis mode at 4891Hz.
- Y-axis mode at 6533Hz.
- Z&Y-axis mode at 11932Hz.
- X&Y-axis mode at 22860Hz.

These four eigenmodes will boost the movement in a particular axis when a current is injected at that frequency. For the magnetometer devised in this work, the objective is the detection of magnetic fields in the X or Y direction so, according to Fleming's right-hand rule [51], a boost in the Z-axis direction is the main and only factor to consider when determining the eigenmodes. The rest of the frequencies should have at least a 1KHz difference from the Z-axis frequency.

4.5 Simulations

With some of the variables being already established, the bulk of the simulations can be taken into action. Taking into consideration the formulas from this work, in table 6 a link between the remaining variables and their effect on the physical properties of the device is exhibited. This table takes into consideration the variation of the objective parameters when there's an increase in certain structural properties. From here on out most simulations were made with the adaptation of table 6 to a 20 nT magnetic field.

Table 6. Correlation between the objective parameters of the device and the structural increase of its properties. Green representing positive effects, red negative, and yellow neutral.

	Parameters									
Increase in:	Q	b	k	m	f_0	ΔC	C0	BW	R	Noise
Spring Width	↓	≈	↑	≈	↑	≈	≈	↓	↓	≈
Spring Height	↓	≈	↑	≈	↑	≈	≈	↓	↓	≈
Spring Length	↑	≈	↓	≈	↓	≈	≈	↑	↑	↓
Number of Plates	↓	↑	≈	↑	↓	↑	↑	≈	≈	↑
Plates Height	↓	↑	≈	↑	↓	≈	↑	↓	≈	↑
Number of CCBs	↓	≈	↑	↑	↓	≈	≈	↑	≈	↓

The achievement of the objectives of this work relies heavily on the balance between the capacitance gained from changing the height and number of parallel plates and the adaptable factor of the springs. The number of CCBs is extremely important due to being the main factor in reducing the thermomechanical noise that rapidly increases when more parallel plates are added.

4.5.1 Early Simulations

The first simulations were made with a single CCB with parallel plates directly attached to the Lorentz bar. The objective was to simply test the structure of the current carrying bar and the effect of the adjustment of some of its variables. In figure 15 a simplified model, as well as an AutoCAD 3D version of the design, is shown.

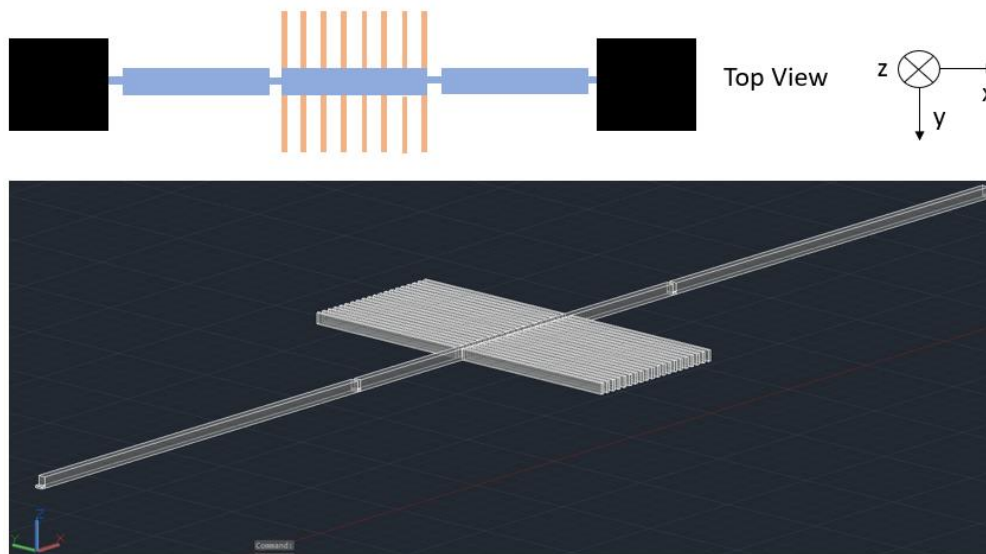


Figure 15. Simplified (Up) and AutoCAD (Down) version of Magnetometer with 1 current carrying bar.

Several experiments were done but are mostly unsatisfactory due to several reasons:

- Parallel plates attached directly to the Lorentz bar increased, unnecessarily, the stiffness of the object.
- The thermomechanical noise was too high.
- Problems with resonant frequencies (different modes being too close).

From formula (3.15) the simplest way to decrease the thermomechanical noise is to increase the number of CCBs. This has the intended effect but increases, substantially, the stiffness of the device which must be compensated by the springs. Regarding the parallel plates, a supporting structure was attached to the Lorentz bar on a single point to limit its interference with the stiffness of the current carrying bar. Figure 16 shows a model of a magnetometer with two Lorentz bars. In this model, the detachment of the parallel plates from the Lorentz bar was applied and proven to be effective.

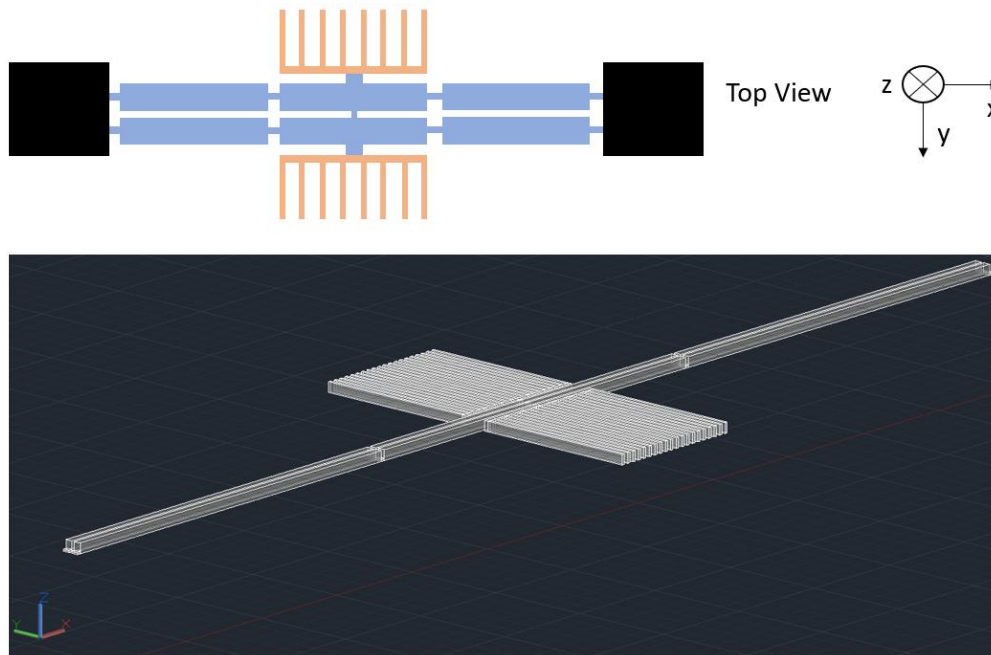


Figure 16. Simplified (Up) and AutoCAD (Down) versions of the magnetometer with 2 current carrying bars with detached parallel plates.

Table 7 shows a series of simulation tests done on the magnetometer where a Lorentz force is generated by a 20nT field when a 4mA current is applied to the magnetometer. A total of 70 parallel plates with a height of 25 μm were attached to the magnetometer. The size (length-width-height) of the Lorentz bar was fixed to 3000 \times 18 \times 25 μm^3 and the Lever-like bars to 500 \times 18 \times 25 μm^3 . A reminder that the frequency of operation of the device is 4952 Hz. The objective of this experiment was to achieve a ΔC higher than 1aF.

Table 7. Two CCBs magnetometer tests in COMSOL and MATLAB with a fixed number of plates and, Lorentz and lever-like sizes. SL, SW and SH represent the length, width and height of the spring.

Test	Spring parameters (μm)			Physical Properties					
	SL	SW	SH	R (Ω)	f_0 (Hz)	Δf (Hz)	BW (Hz)	ΔC (aF)	Noise (nT/ $\sqrt{\text{Hz}}$)
1	5	18	5	64.6	5398	446	855	0.02	3.03
2	8	18	5	84.6	5083	131	260	0.07	3.02
3	9	18	5	91.3	4996	44	88	0.22	3.02
4	9.3	18	5	93.3	4968	16	33	0.58	3.02
5	9.4	18	5	94.0	4960	8	16	1.2	3.02

The results from the experiment were quite good since the target ΔC and Resistance were achieved but several problems surfaced. For once when the ΔC stood above 1aF the bandwidth of the system was at 16 Hz bandwidth which is subpar from the 50 Hz stipulated objective. Another problem is the noise that throughout the experiment stood above the 3 nT/ $\sqrt{\text{Hz}}$ noise limit. So, for the next set of simulations, it was set the objective of reducing the noise and increasing the bandwidth. To achieve this, the number of CCBs was increased to three and the number of parallel plates was increased to 140. Figure 17 shows the result of this addition.

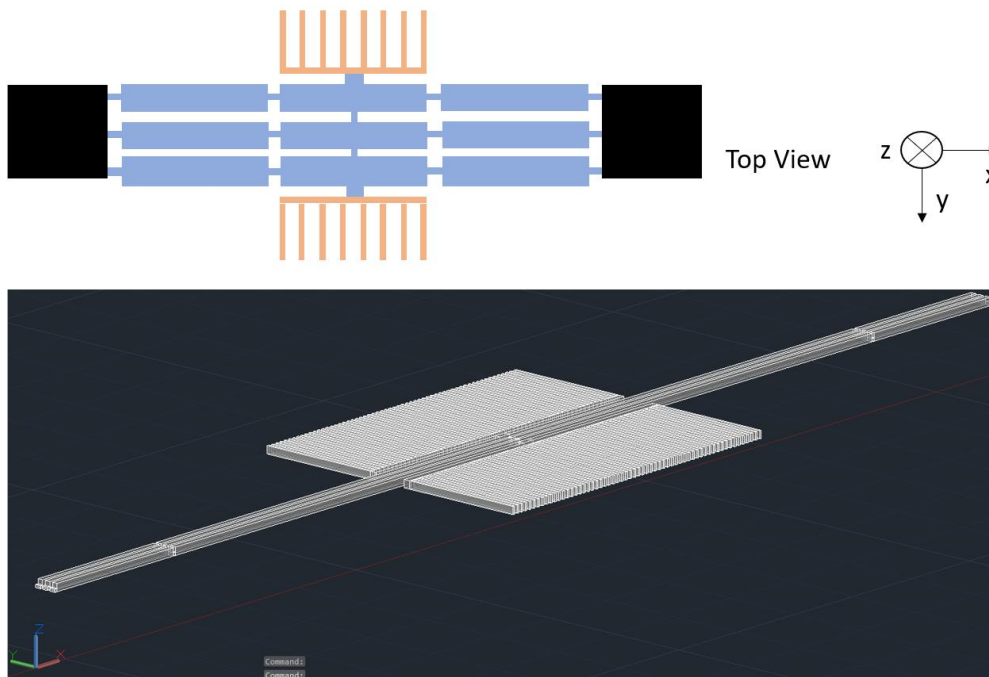


Figure 17. Simplified (Up) and AutoCAD (Down) version of Magnetometer with 3 current carrying bars with the detached parallel plates.

A similar experiment to the earlier one from Table 7 was conducted the only difference being the number of parallel plates increasing to 140 and the extra CCB. This time the objective was to achieve a bandwidth of 50Hz while maintaining the 1 aF ΔC and achieving a thermomechanical noise lower than 3 nT/ $\sqrt{\text{Hz}}$. Table 8 shows the results of the trial.

Table 8. Three current carrying bars magnetometer tests with a fixed number of plates and, Lorentz and lever-like sizes. SL, SW and SH represent the length, width and height of the spring.

Test	Spring parameters (μm)			Physical Properties					
	SL	SW	SH	R (Ω)	f_0 (Hz)	Δf (Hz)	BW (Hz)	ΔC (aF)	Noise (nT/ $\sqrt{\text{Hz}}$)
1	9.5	18	5	94.6	5068	116	230	0.14	2.85
2	10	18	5	98.0	5008	56	111	0.30	2.84
3	10.25	18	5	99.6	4977	25	50	0.67	2.84
4	10.3	18	5	100.0	4972	20	40	0.84	2.84
5	10.5	18	5	101.3	4949	3	5	5.82	2.84

In this test, the 50 Hz and the noise targets were achieved but the ΔC dropped considerably when the 50 Hz mark was achieved. An important parameter that was gathered from this experiment was that to achieve a bandwidth of 50 Hz the Δf must attain the target of around 26 Hz. This implies that, for the final magnetometer, the target resonance frequency must be just about 4977 Hz. A similar experience was also done where the number of parallel plates was increased to 160 to see if the target ΔC was achieved but that goal was a little off and the noise went above 3 nT/ $\sqrt{\text{Hz}}$. These results are shown in Table 9.

Table 9. An additional test to a three CCB magnetometer where the number of fixed plates was increased to 160.

Test	Spring parameters (μm)			Physical Properties					
	SL	SW	SH	R (Ω)	f_0 (Hz)	Δf (Hz)	BW (Hz)	ΔC (aF)	Noise (nT/ $\sqrt{\text{Hz}}$)
1	10.25	18	5	99.6	4872	80	160	0.22	3.04
2	9.45	18	5	94.3	4973	21	42	0.85	3.04

From here another Lorentz bar was added to further reduce the noise. Some problems with the design of the structure started to appear where the addition of another Lorentz bar started to increase the stiffness to considerable levels and the natural frequencies of the device started to overlap.

Figure 18 displays an eigenfrequency simulation of a three CCB magnetometer where the device shows a Y-axis eigenmode at 4026 Hz and a Z-axis eigenmode at 4976 Hz. From here two major problems arise. The first one is the Y-axis natural frequency coming at a lower frequency than the X-axis and the second one is that the difference between both frequencies is lower than 1 KHz. This will result in significant interference to the Z-axis movement of the magnetometer as the X-axis movement will also suffer some gain when injecting a current at the target frequency.

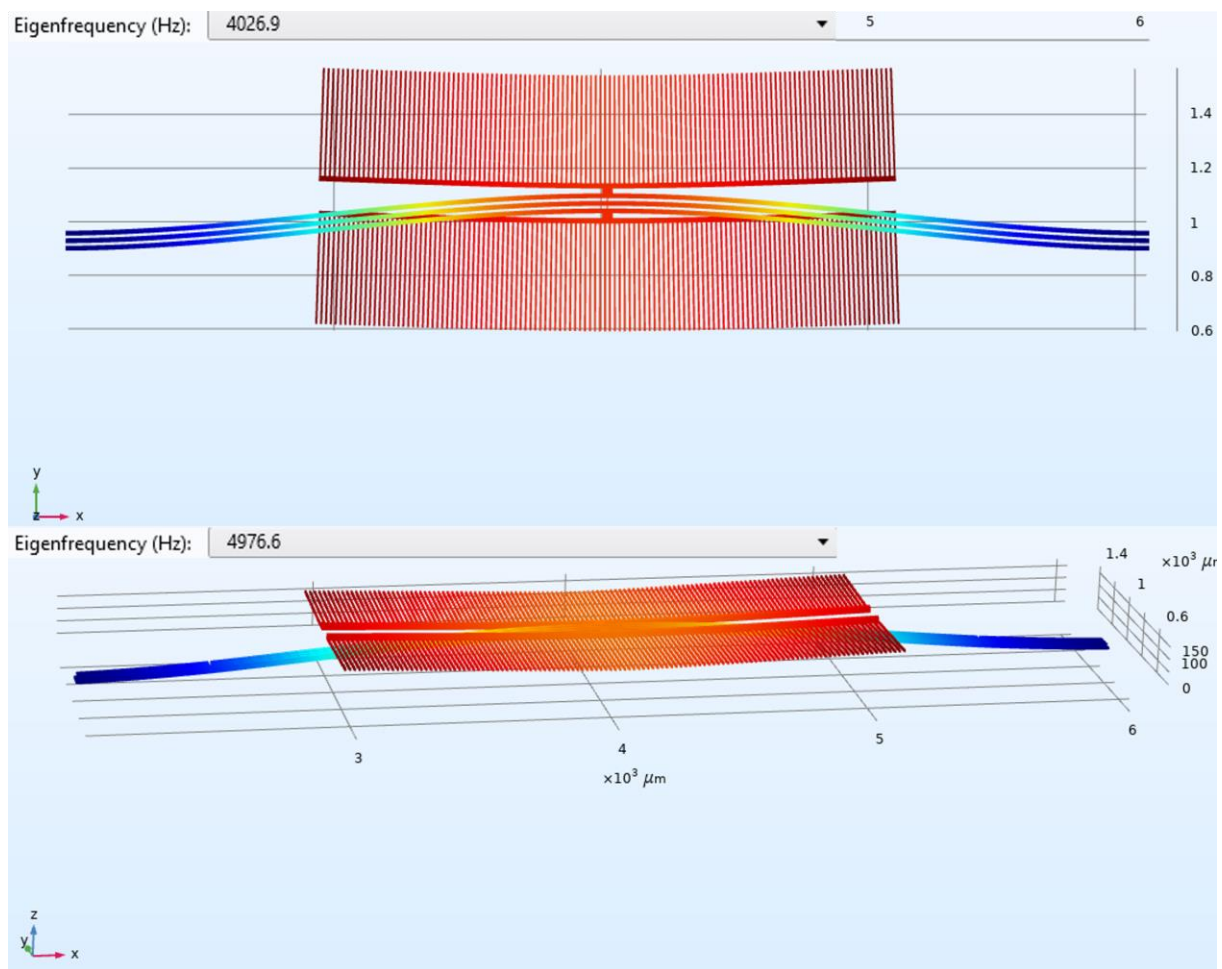


Figure 18. 3 current carrying bar magnetometer eigenfrequency test. The top image represents the first eigenmode at 4026 Hz with a displacement of mass at Y-axis. The bottom figure represents the second eigenmode at 4976Hz with a displacement of mass in the Z-axis.

Since the device more easily moves in the Y-plane, hence a lower natural frequency, some changes must be made to make sure that the natural frequency for the eigenmode that boosts the Z-axis movement is

the first to appear in the simulation and the other eigenmodes have to be, at least, 1KHz higher. Another problem that can be seen in figure 18 in the bottom image is that when the bar that supports the parallel plates reaches the maximum z displacement the parallel plates at the edge of the supporting bar move further when compared to the plates in the middle. Even though this may have some advantages, for the purpose of all mathematical models corresponding to reality, the height displacement of all parallel plates should be equal in all instances. Fixing these issues requires changes to the whole magnetometer structure.

A set of final experiments was attempted to reduce the resistance of the current carrying bars. To achieve this, the width of the springs and the other structures of the current carrying bar were matched and the length of the springs was fixed to $5\mu\text{m}$ making the only available parameter of adaptation the height of the springs. The Lorentz bar had a length-width-height of $3000 \times 18 \times 25 \mu\text{m}^3$ and the lever-like bars $500 \times 18 \times 25 \mu\text{m}^3$. Table 10 shows the results where it's possible to see a successful resistance reduction.

Table 10. Resistance test where CCB represents the current carrying bars and the parallel plates (PP)

Test	Spring parameters (μm)			Structure		Physical Properties					
	SL	SW	SH	CCB	PP	R (Ω)	f_0 (Hz)	Δf (Hz)	BW (Hz)	ΔC (aF)	Noise (nT/ $\sqrt{\text{Hz}}$)
1	10	18	5	2	70	98.0	3952	999.3	230	0.01	3.03
2	5	18	10.3	2	70	47.5	4976	24.6	111	0.40	3.03
3	5	18	10.15	2	70	47.8	4961	9.9	50	0.99	3.03
4	5	18	9.6	3	160	48.7	4975	23	40	1.01	3.06
5	5	18	9.63	3	160	48.6	4977	25.6	5	0.91	3.06

4.5.2 Main structure simulations

The main objective at this point is to fix the existing issues that the magnetometer presents and start reducing the height of the plates. This has many advantages since it doesn't intervene in the variation of capacitance and massively reduces the weight and nominal capacity of the magnetometer. It's also important to maintain in check the $\Delta C/C_0$ ratio for future electrical components. This helps the ability of electrical systems to detect magnetic fields. The greater the ratio, the better.

To fix the extra height gain from the bottom image from figure 18 the movable plates were shifted from the edge of the device to the middle of it. Figure 19 shows a simplified version of this transition where, in the after image, it's shown that the movable plates are placed between the two CCBs with a supporting bar uniting both bars. With this design, when a displacement occurs in the device, all parallel plates will be at the same height in all instances of dislocation. With this alteration, it's made sure that all simulations' mathematical calculations are as close to reality as possible.

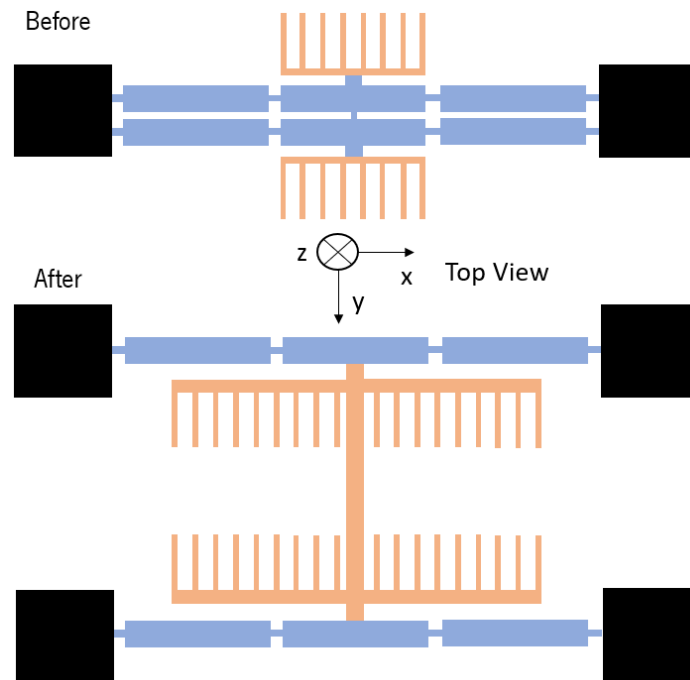


Figure 19. Magnetometer adaptation. Before shows the magnetometer with the parallel attached to the outside of the current carrying bars while the after image parallel plates are attached to the inside.

A simple simulation (table 11) proceeded where a magnetometer with four CCBs and parallel plates height reduction was compared to an earlier simulation (Test 5 table 10). The height of the springs was also matched with the height of the plates. All other structures are the same.

Table 11. Parallel plate height reduction experiment.

Test	Spring parameters (μm)			Structure			Physical Properties		
	SL	SW	SH	CCB	PP	PP Height	Mass (mg)	C0 (pF)	Noise (nT/\sqrt{Hz})
1	5	18	9.63	3	160	25	0.065	13.5	3.06
2	5	18	9	4	160	9	0.035	4.85	1.80

As intended, a massive reduction in all three instances of the physical properties was achieved especially in the thermomechanical noise that was, until now, one of the hardest properties to be lowered. From here on out the height of the parallel plates will always be matched to the height of the spring. This happens due to the fabrication steps requiring that both heights be the same.

With regards to the eigenmodes, to make sure the Z-axis eigenmode is the first to surface in the simulation, the width of the current carrying bars is increased. This alteration will make sure that the movement in the Y-plane is much harder. At this point, the width of the springs is also matched with the rest of the parts of the current carrying bars. With an initial width of $18\mu\text{m}$, a boost to $30\mu\text{m}$ was decided to disregard the effect of the Y-plane eigenmode.

Table 12 shows a succession of tests where most of the concepts explained here were applied. The width of the CCB is $30\mu\text{m}$ in all instances and, apart from the springs, the height is $25\mu\text{m}$. The height of the plates and springs was also fixed at $10\mu\text{m}$. These tests were finetuning for the final device and as shown in the table these were all close to achieving a pass in all categories of the objectives proposed in chapter 3.7 especially tests 4 and 5 which were able to achieve very good results in all categories and had the second eigenmode with a distance of at least 2.5KHz.

Table 12. Main structure tests. LZ-L represents the length of the Lorentz bar and LL-L the length of the lever-like bar.

Test	CCB parameters (μm)			Structure		Physical Properties					
	SL	LZ-L	LL-L	CCB	PP	R (Ω)	f_0 (Hz)	Δf (Hz)	BW (Hz)	ΔC (aF)	Noise ($nT/\sqrt{\text{Hz}}$)
1	36.2	1000	1500	3	100	88.0	4975	26	47.7	0.72	1.88
2	25.9	1000	1500	3	120	67.5	4977	28	50.5	0.68	2.08
3	7.4	1500	1250	3	160	30.4	4978	29	52.5	0.56	2.44
4	43.8	500	1750	4	160	103.2	4977	28	51.0	1.37	1.77
5	38.8	500	1750	4	150	93.2	4977	28	51.8	1.16	1.81

For the final device, a series of small changes were applied so that a fabrication process could be assembled

4.6 Final Device

After several simulations, the device design was closed and used for fabrication. The final parameter as well as the results can be seen in table 13. All proposed objectives in chapter 3.7 were achieved with some margin, especially in the capacity variation department where a considerable difference from the objective was noted. All simulations were made with a 20nT field, 1mBar pressure and an operating frequency of 4952Hz.

Table 13. Final magnetometer values divided between structural and physical parameters for a 20nT magnetic field at 1mBar pressure.

Structural Parameters	Value	Physical Parameters	Value
Lorentz Bar (width×height×length)	30×25×500 μm^3	R	100.2 Ω
Lever-Like Bar (width×height×length)	30×25×1750 μm^3	BW	50.1 Hz
Springs (width×height×length)	30×10×42,3 μm^3	Noise	1.77 $\text{nT}/\sqrt{\text{Hz}}$
N° Parallel Plates	160	ΔC	1.37 aF
Parallel Plate height	10 μm	C0	5.38 pF
N° Current carrying bars	4	f_0	4976.7 Hz

Figure 20 shows a simplified top view model of the magnetometer where it's divided into two sections. Represented in blue are the current carrying bars and in orange are the parallel plates system. It also shows a 3D model of the movable components of the device that was used in the simulation. The method applied in the parallel plate system is the same as the one described in chapter 4.3.

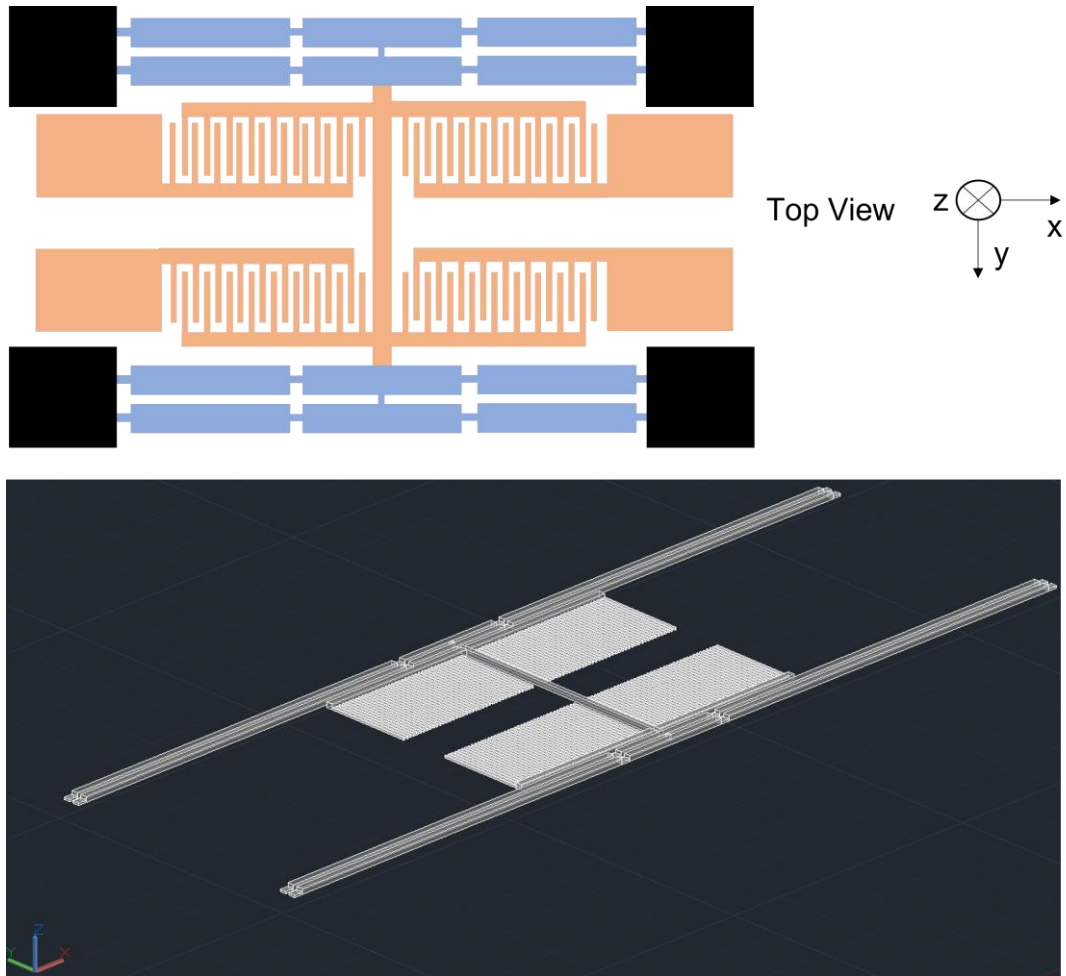


Figure 20. Simplified (Top) and 3D model (Bottom) view of the magnetometer model that was used in this work.

When determining the eigenmodes of the device the Z-plane mode was ascertained to be at a frequency of 4976.7Hz with the next closest natural frequency situated at 8633.8Hz. This gives a secure difference in frequencies to be able to make sure that there won't be any other interferences from separate eigenmodes apart from the one that helps the movement in the Z-axis. Figure 21 shows the result of the simulation.

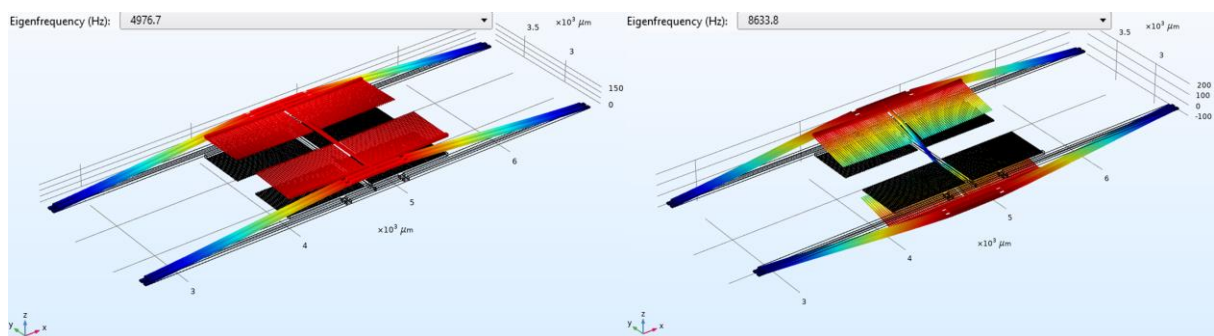


Figure 21. Eigenmode test of the final structure. On the left Z-axis eigenmode at 4976.7Hz and on the right Z&Y-axis eigenmode at 8633.8Hz.

5. MICROFABRICATION

With the model of the magnetometer ready to be used, a fabrication runsheet is drawn. In this chapter, a brief explanation of the fabrication techniques and the following fabrication steps is laid down. The substrate of the magnetometer is a single-side polished silicon-on-insulator (SOI) wafer, its constitution can be seen in the following figure:



Figure 22.Simplified Silicon Wafer Layers

From top to bottom (thickness) with a diameter of 8 inches (20,32cm):

1. Device Layer: 25 μ m Silicon.
2. BOX (sacrificial buried oxide): 2 μ m SiO₂ (Silicon dioxide).
3. Handle: 650 μ m Silicon + 2 μ m SiO₂.

To finalize the chapter, the various device layout models as well as the results from the fabrication are revealed.

5.1 Cleanroom

All fabrication steps and processes at INL are done in a cleanroom. This is a built space that has a very low concentration of airborne particles. To achieve this the room has to be isolated, ventilated and actively cleansed to attain a controlled space from contamination since, in several processes, a single speck of dust could compromise an entire fabrication process. Additionally, all personnel that steps into the cleanrooms has to wear suits to contain dust spread and, upon entry, go through an air shower to be cleansed from particles. Cleanrooms are also, normally, divided into two subsections one where the lighting is normal and another with a special light to not interfere with photolithography processes.

Cleanrooms are also subdivided into cleanliness levels that are quantified by the number of particles per cubic meter with consideration of the size of said particles. For example, according to the International Organization for Standardization (ISO) 14644-1:2015 standard [52], an ISO class 7 cleanroom doesn't

allow more than 2930 particles above 5 μm per cubic meter. The lower the ISO class the cleaner the cleanroom.

At INL there are two ISO class areas. The photolithography area is ISO 5 and the other areas are ISO 6. Its properties can be seen in table 14.

Table 14. ISO cleanroom standards 5 and 6.

Class	Number of Particles per Cubic Meter by Micrometre Size (μm)					
	0.1	0.2	0.3	0.5	1	5
ISO 5	100,000	23,700	10,200	3,520	832	29
ISO 6	1,000,000	237,000	102,000	35,200	8,320	293

5.2 General microfabrication techniques

5.2.1 Lithography

Lithography is a technique that uses incident radiation to produce patterned thin films of a material, the usual being photoresist in the IC industry, over a substrate, standard silicon wafer. The resist is deposited normally after a prime treatment on a wafer substrate using spin-coating. This serves the objective of partially protecting the surface of the wafer when using other techniques such as etching or deposition of other materials. The result of the interaction between the radiation and the resist depends on its type. If it's a positive resist, when exposed to radiation the resist will soften. On the contrary, if it's negative it will harden the resist. This is used to "draw" complex structures on top of the wafer. Figure 23 shows a simplified three-step process for this lithography. The first step is the spin-coating of the wafer with resist. Next, the wafer is sent to an aligner, stepper or laser write for exposure where each layer requires a different mask until the surface of the wafer is exposed. Lastly, the wafer is developed where the exposed photoresist is removed with a solvent passing through a baking step to ensure the exposed material adheres to the wafer[53].

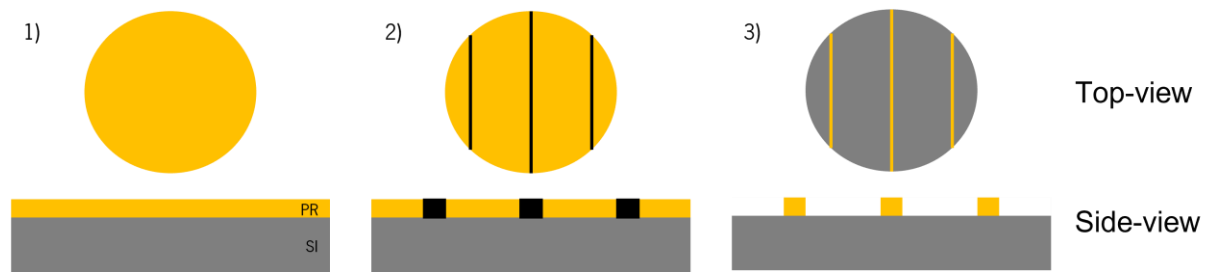


Figure 23. Optical lithography process of negative resist. 1) Photoresist deposition. 2) Exposure. 3) Development.

5.2.2 Metal deposition and etching

The metal deposition is done through a sputter deposition process which is a physical vapour deposition technique for thin films on substrates through the phenomenon of sputtering. This technique is based on the ion bombardment of the source material. This will result in vapour due to a physical process.

The process used at INL is called magnetron sputtering which is a high-rate vacuum coating technique for the deposition of metal, alloys and compounds [54] with thicknesses up to a millimetre. This procedure is based on the formation of plasma near the surface of the target material, that'll result in the formation of argon ions. Resultant ions are accelerated to the target material and bombard the surface so that particles are released from it. The resulting released particles are then deposited in the form of a film on the substrate[55] (figure 24). Direct-Current (DC) power can be used to deposit metals while semiconductors and isolators require either Radiofrequency (RF) power or pulsed DC. In the case of this work the metal to be deposited is AlSiCu which is an aluminium, silicon, and copper alloy.

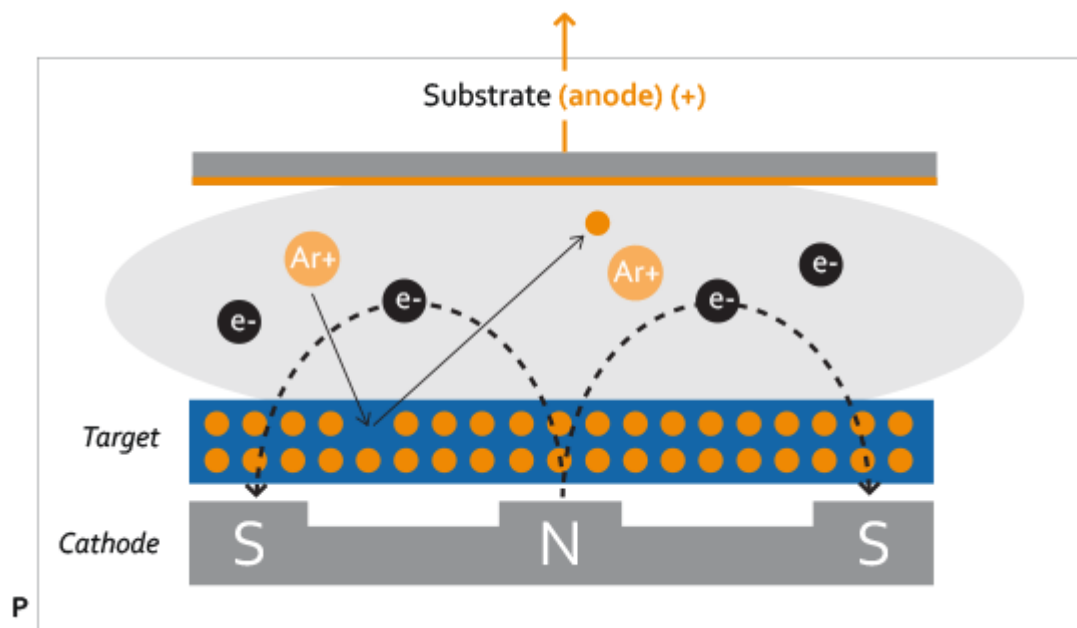


Figure 24. Magnetron Sputtering Process. Adapted From [56].

The etching of the metal is done through an aluminium wet chemical etchant [57]. This chemical has selectivity toward materials containing aluminium which is the case of AlSiCu. Even though the etch rate, when it comes to the other materials on the wafer, is still present, it pales in comparison with the AlSiCu etch rate. Usually, depending on the etch rate, the wafer is submerged in the chemical for a calculated time and then rinsed with water.

5.2.3 Grayscale Lithography

Grayscale lithography (GS) is a fabrication technique that enables the construction of three-dimensional (2.5D, in fact) structures in the photoresist; as opposed to conventional, binary, lithography. Through the usage of spatially modulating ultraviolet dosage, one can vary the depth at which the photoresist is developed [58]. This enables the creation of masks with multiple levels of photoresist thickness. In this lithography technique, the photoresist layer is exposed using a lateral variation of the exposure dose using an intensity-controlled laser beam. Figure 25 shows a simplified GS process where three different sections of the photoresist are hit with different laser intensities resulting in a complex topology after development.

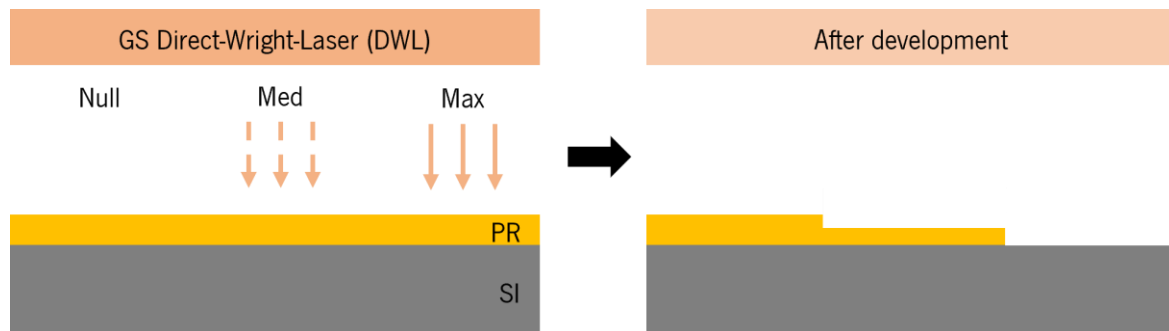


Figure 25. GS process with three (Null, medium and maximum) different laser intensities. PR refers to the photoresist layer and Si to the silicon. Adapted from [59].

This technique allows for the patterning of perfectly aligned asymmetric structures that enables, in the case of this work, the differentiation between two different heights of the device (25 μ m structures such as the lever-like and Lorentz bars and the 10 μ m structures like the springs and the thinned parallel plates). This procedure bypasses many misalignment problems due to not requiring extra lithography steps that would incur problems such as alignment marks quality problems [59].

5.2.4 SiO₂ deposition and etching

At INL, the deposition of SiO₂ is accomplished through plasma-enhanced chemical vapour deposition or PECVD which is a derived process of chemical vapour (CVD) deposition that's a method to produce high-quality thin films on a substrate. In CVD the heated substrate (wafer) is exposed to one or more volatile compounds of the to-be deposited material that'll chemically react with other gases inside a reactor giving birth to a non-volatile solid. This solid will then be conformally deposited on the surface of the wafer. PECVD uses a plasma created by radio frequency to enhance the chemical reaction rates of the precursors allowing for the deposition of thin films at lower temperatures [60] when compared to conventional CVD [61]. Figure 26 shows the image of a PECVD reactor where the deposition process can be seen.

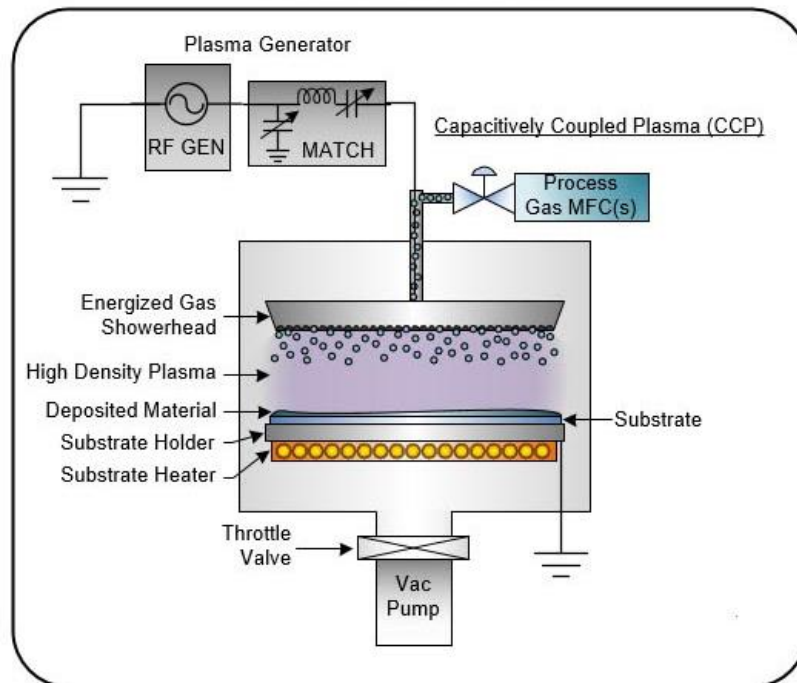


Figure 26. Diagram of PECVD process reactor. Adapted from [61].

The etching of SiO₂ is achieved with reactive ion etching (RIE) which is a type of dry etching that uses chemically reactive plasma to remove material from the top of wafers. In this type of etching, ions are accelerated towards the substrate clashing with the exposed material and removing it. In RIE there are two types of directional etch: Anisotropic and isotropic. Anisotropic, in dry etching, refers to vertical etched sidewalls whereas isotropic means spherical sidewalls which are the result of equal vertical and horizontal etching rates [62] as shown in figure 27.

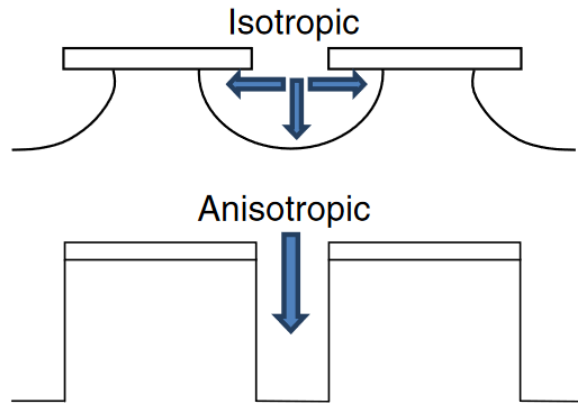


Figure 27. Schematic of isotropic and anisotropic plasma etching. Taken from [62].

In the case of this work, anisotropic etching is utilized that's obtained when sufficient sidewall passivation takes place during the etching process [62].

5.2.5 Silicon etching

In this work the silicon etching will be done through a process called deep reactive ion etching (DRIE) which is a subclass of the RIE. It can be seen as an improvement of the already talked about RIE in the sense that it drastically improves the results with its deep, steep-sided features in wafers with aspect ratios (etch depth/feature width) beyond 10:1 [63]. In the case of DRIE, several gases, as well as the substrate, are introduced inside a reactor where plasma is introduced that breaks the gas into ions. These ions are then accelerated towards the surface of the wafer etching, anisotropically, the material on the surface. In the case of this work, a high-rate DRIE process for silicon is used called the Bosch process [64] which can be resumed in the repetition of small isotropic etches to achieve an anisotropic trench. Figure 28 shows the three-step cycle that this technique consists of: The first step is the film deposition where a passivation film is deposited on the sidewalls and bottom of the trench, usually, the deposited gas is Octafluorocyclobutane (C_4F_8). This layer protects the entire substrate from further chemical attack and etching. The second step is the bottom film etching where the passivation film on the bottom of the trench is etched. Lastly, the third step is the silicon etch where only the material on the bottom is removed. The gas used in both etching steps is, often, sulphur hexafluoride (SF_6) which is an isotropic gas. This cycle is then repeated until the desired depth is achieved. With this three-step cycle exceptional deep trenches are achieved with exquisite anisotropy, etch-rate and etch mask selectivity[65].

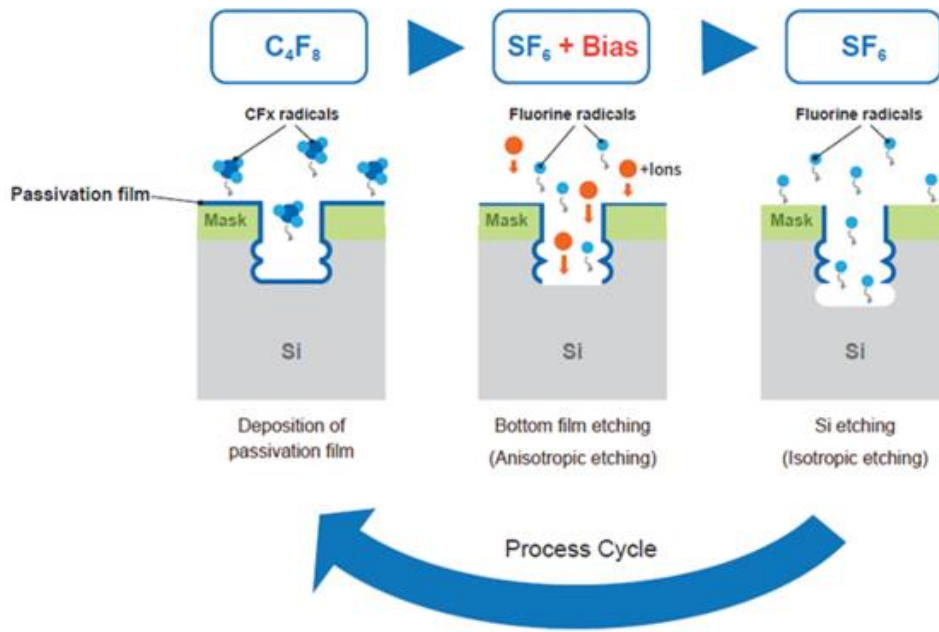


Figure 28. Principles of the Bosch Process. Adapted from [65].

5.3 MEMS magnetometer process flow

The fabrication of the magnetometer is a complex development that must be divided into several steps in a specific order to achieve a magnetometer with the utmost resemblance to the simulation. According to figure 29, these steps can be divided into the following list as per the runsheet:

1. Frontside metal deposition and patterning followed by SiO₂ deposition.
2. Frontside Grayscale lithography and SiO₂ etch.
3. Backside Lithography and SiO₂ etch.
4. Frontside Silicon Etch.
5. Backside Silicon Etch and structural release.

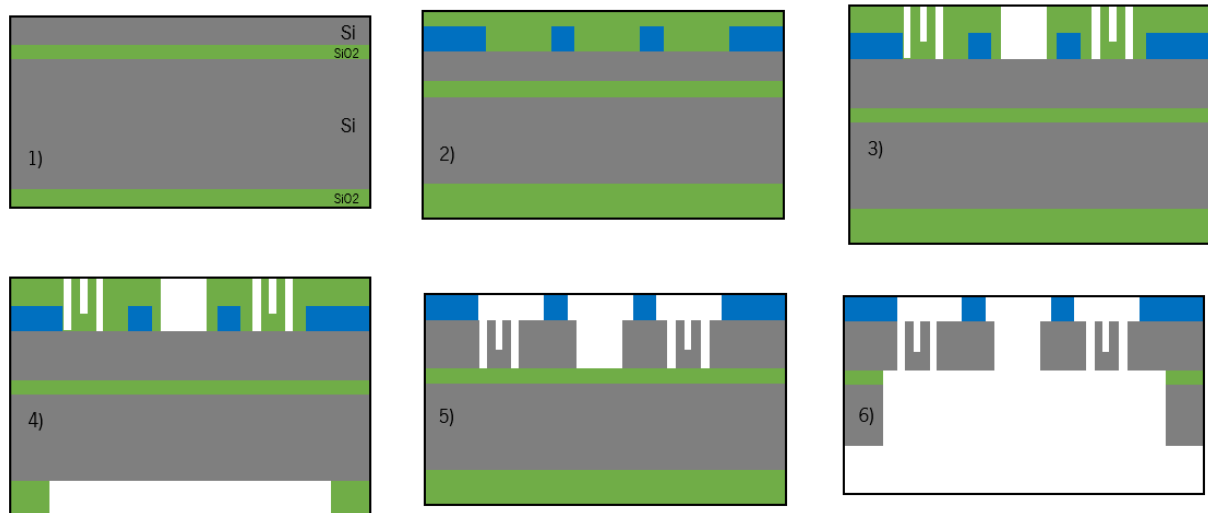


Figure 29. Magnetometer Fabrication Process. 1) SOI wafer. 2) Metal Deposition and Patterning and SiO2 deposition. 3) Frontside Grayscale lithography and SiO2 etch. 4) Backside lithography and SiO4 Etching. 5) Frontside Silicon Etch. 6) Backside Silicon Etch and structural release.

Each of these steps will be further discussed in the following sections. Additionally, the reason the springs can't be covered in metal is due to the deposition of the metal being earlier than the frontside etch where the springs are carved upon the magnetometer.

5.3.1 Frontside metal deposition and patterning and SiO2 deposition

The first set of steps of the fabrication is the deposition and patterning of a 500nm metal layer on the front side of the wafer. This is divided into three steps:

1. Metal deposition. The first step goes through a 500nm deposition of AlSiCu by magnetron sputtering of the wafer. This is done after a pre-etch to increase adherence. This process is performed through a physical vapour deposition machine Timaris FTM [66].
2. Lithography. This process has several substeps: First, there's the coating of the resist through an Optical Track [67] where the photoresist (PR) will be deposited through spin-coating on the front side of the wafer. Then the PR will be patterned in a laser-based maskless optical lithography system with a dark polarity [68]. And lastly, the PR will be developed in the optical track leaving open to metal etching the structure where metal isn't supposed to be.
3. Metal etching. This phase will be processed on a wet bench [69] where the exposed (not covered with resist) AlSiCu area will be chemically attacked until no metal remains on top of the silicon exposed area. The wafer will then go to a plasma asher [70] to remove the remaining resist.

At the end of these three steps, a patterned metal structure will sit upon the silicon with a patterning defined by a mask that will be later shown. Figure 30 shows the three-step process explained earlier.



Figure 30. Simplified metal layer processes. 1) Deposition of AlSiCu and PR. 2) PR patterning and development. 3) Metal chemical etching and resist strip.

To finalize this step a $2\mu\text{m}$ thick SiO_2 layer will be deposited by PECVD [71] on both the frontside and backside of the wafer. Figure 31 shows the result of the deposition.

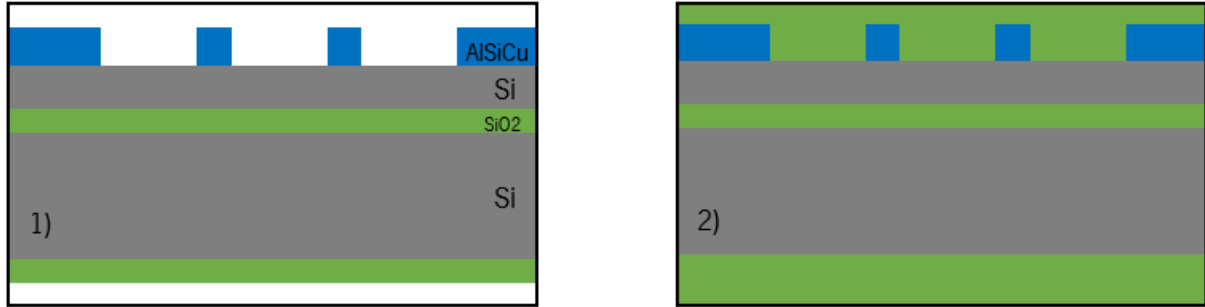


Figure 31. Frontside and backside PECVD SiO_2 deposition process. 1) starting wafer. 2) SiO_2 deposition.

5.3.2 Frontside Grayscale lithography and SiO_2 etch

In this work, GS lithography is used to attain three different heights on the magnetometer. In the final device from section 4.6 it's shown that the magnetometer has 3 different sections: One with $25\mu\text{m}$ of silicon (Lever-like and Lorentz bars for example), another with $10\mu\text{m}$ (springs and parallel plates) and others with no silicon (the delimitation of the capacitor plates and the areas where the magnetometer is free to move for example). To achieve this, the properties of GS are used to draw in the SiO_2 sections where these heights are differentiated. To avoid alignment issues all these different areas must be drawn in a single lithography. This is possible due to a technique developed by Inês Garcia et al. [59] where, through the use of GS lithography, areas with 3 different heights are drawn in the resist. Figure 32 shows a simplified GS process.

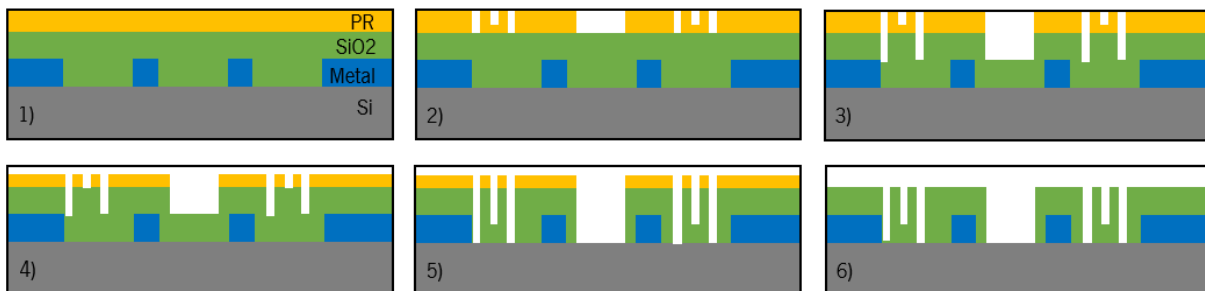


Figure 32. Simplified frontside grayscale process. 1) Photoresist deposition. 2) Grayscale patterning and photoresist development. 3) SiO_2 RIE etching. 4) Partial photoresist stripping. 5) SiO_2 etching. 6) Photoresist removal.

The procedure is divided into 6 steps:

1. Coating of photoresist, by an optical track, on top of the SiO₂ that was placed at the end of the last section.
2. With the use of the Grayscale lithography properties in a direct write laser (DWL) [68], two areas are struck with different laser intensities. One where the resist will be attacked and developed for its whole height (Higher laser intensity) and another for half its height (Lower laser intensity).
3. SiO₂ RIE etching [72] until it reaches a certain height.
4. Partial resist strip revealing previously covered SiO₂ area.
5. SiO₂ RIE etch.
6. Photoresist removal.

In the end, there will be 3 different heights of SiO₂ that can be used to carve the structure onto the silicon. This is the method to be able to obtain the thinned and non-thinned parallel plates as well as the tinned springs.

5.3.3 Backside Lithography and SiO₂ etch.

Since the backside of the wafer is also covered with SiO₂, a lithography is necessary to reveal the area where the backside silicon has to be etched. This area is called the Trench and it's also used in the frontside to delimit the areas where the magnetometer is supposed to be free of movement. Figure 33 shows the three-step backside process where the photoresist is deposited, exposed and developed and then the SiO₂ is etched revealing the area where the silicon will be carved



Figure 33. Simplified backside SiO₂ etching. 1) Photoresist deposition. 2) Photoresist patterning and development. 3) SiO₂ RIE etching.

5.3.4 Frontside Silicon etching

After all these steps the wafer is ready for the silicon to be etched. Figure 34 shows the process of etching the frontside silicon of the wafer. The objective of this stage is to carve the complete magnetometer silicon structure upon the 25 μ m thick silicon of the wafer.

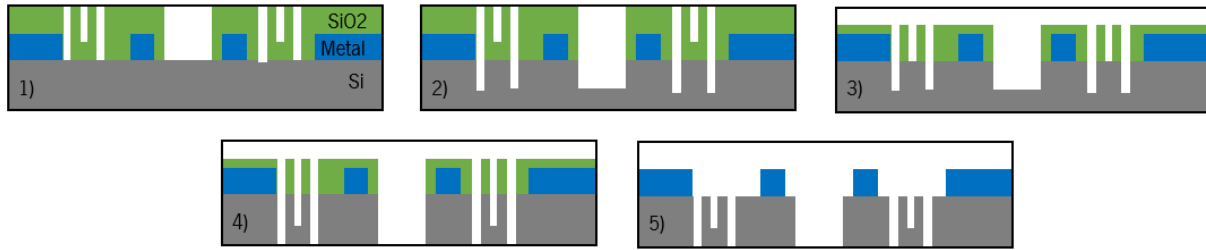


Figure 34. Simplified frontside silicon etching. 1) Initial wafer. 2) Silicon DRIE etching. 3) SiO2 RIE Etching. 4) Silicon DRIE etching. 5) SiO2 removal and cleaning.

This process can be divided into four steps as per figure 34:

1. Partial silicon DRIE etching (10 μ m) [73] on the current wafer. The presence of SiO₂ on top of some of the structures won't allow the protected silicon to be etched.
2. Partial etching of SiO₂ by RIE until the other silicon structures are revealed and wafer cleaning on a wet bench due to debris from DRIE.
3. Partial silicon etching (around 15 μ m) by DRIE.
4. Removal of the remaining SiO₂.

At the end of this process, a detailed magnetometer should be seen in the inspection ready for backside etching and structure release.

5.3.5 Backside Silicon etch and release

Finally, as the last step, a procedure to remove the backside silicon and structural release can be observed in figure 35. First, the silicon on the backside is attacked by DRIE revealing the BOX layer in the middle of the wafer. Lastly, the structures are released using hydrogen fluoride (HF) vapour etching that consumes the BOX layer and the remaining SiO₂ present in the device.

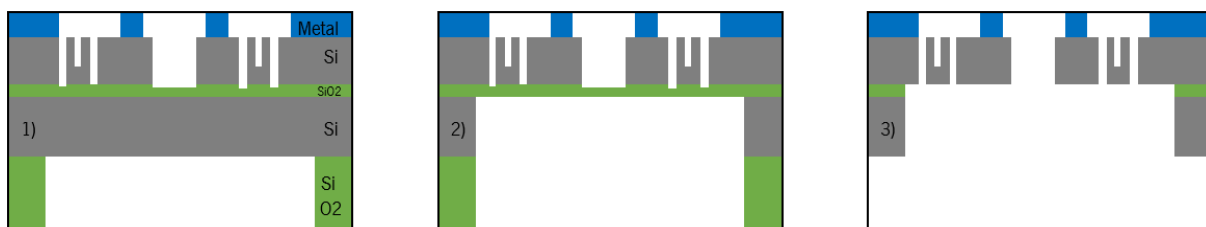


Figure 35. Simplified backside etching and release. 1) SOI structure. 2) Silicon DRIE etching. 3) BOX and remaining SiO₂ etching.

5.4 Layers Design

Now that the microfabrication process sequence is defined, the masks that required for the different lithographies must be drawn. This was done through the combination of Autocad and KLayout which is used to visualize and draw masks. The layers that will be needed are the following:

- 25 μ m structures layer – GS1 – Grayscale max-height – Lorentz and Lever-like bars, contacts, non-thinned parallel plates and supporting structures.
- 10 μ m structures layer – GS2 – Grayscale second height – Springs and thinned parallel plates.
- 0 μ m layer – GS3 – Grayscale max-depth – Zones with no silicon.
- Metal patterning – METAL – Contacts, Lorentz and Lever-like metal paths and structure names.
- Trench Layer – TRENCH – This is especially important to determine the silicon etching on the backside of the wafer.

The following sections will be a simple showing of the drawn masks and their peculiarities.

5.4.1 GS1

Figure 36 shows the KLayout design for GS1. As referenced before GS1 represents the structures of the magnetometer that have a height of 25 μ m. From the image, the current carrying bars can be seen, except for the springs, with their adjacent contacts where the current flow will be induced. On the parallel plates, the remaining 25 μ m plates that will serve as distinguishers if the magnetometer is going up or down can also be found. The contacts for the 25 μ m and 10 μ m high parallel plates can also be recognized. Two adjacent structures called stoppers are added to the whole structure so that the magnetometer won't oscillate in the up/down direction.

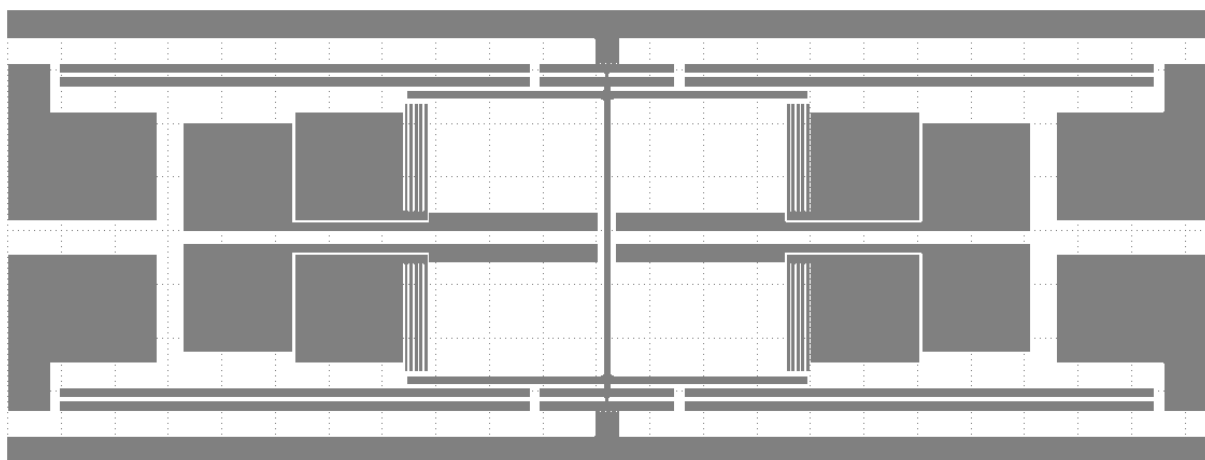


Figure 36. GS1 mask structure KLayout model.

5.4.2 GS2

Figure 37 shows both GS1 and GS2 designs. This is so that the complementary $10\mu\text{m}$ structures can be seen following its $25\mu\text{m}$ counterpart. The only structures present in GS2 are the 4 springs per current carrying bar and the intercalated parallel plates that make up the capacitance detection method.

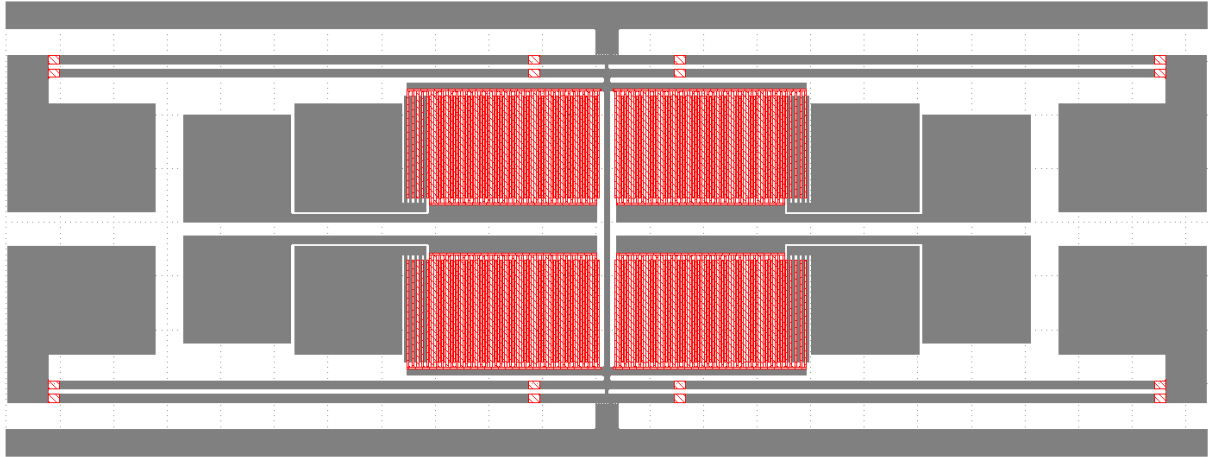


Figure 37. GS1 and GS2 masks KLayout model.

5.4.3 GS3

Figure 38 shows GS3 design. This structure represents the opposite of both GS1 and GS2 masks and is the magnetometer zones that don't have any silicon. This mask is very important for grayscale lithography to define the zones where the laser is at its highest intensity.

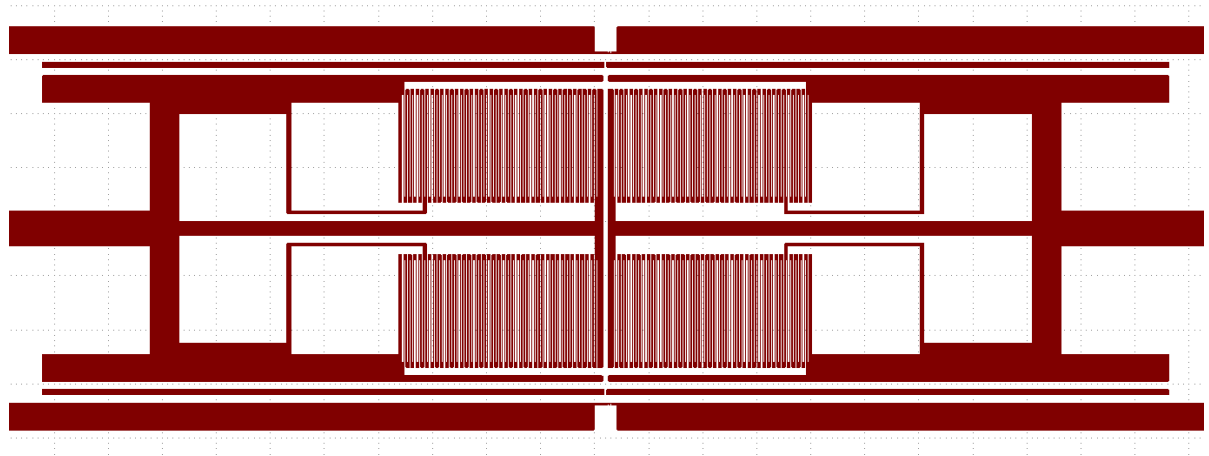


Figure 38. GS3 mask structure KLayout model.

5.4.4 METAL

Figure 39 shows both the GS1 and METAL designs. The METAL mask will be the first to be used for the metal deposition and patterning. The areas that it covers are the contacts, the current carrying bars and

small squares on top of the stoppers that serve as orientation guides. Each magnetometer will also have a number associated with it that represents its version as well as a small description of the device that includes the gap between the parallel plates and the added overextension of the width of the parallel plates due to an over-etch process that can occur.

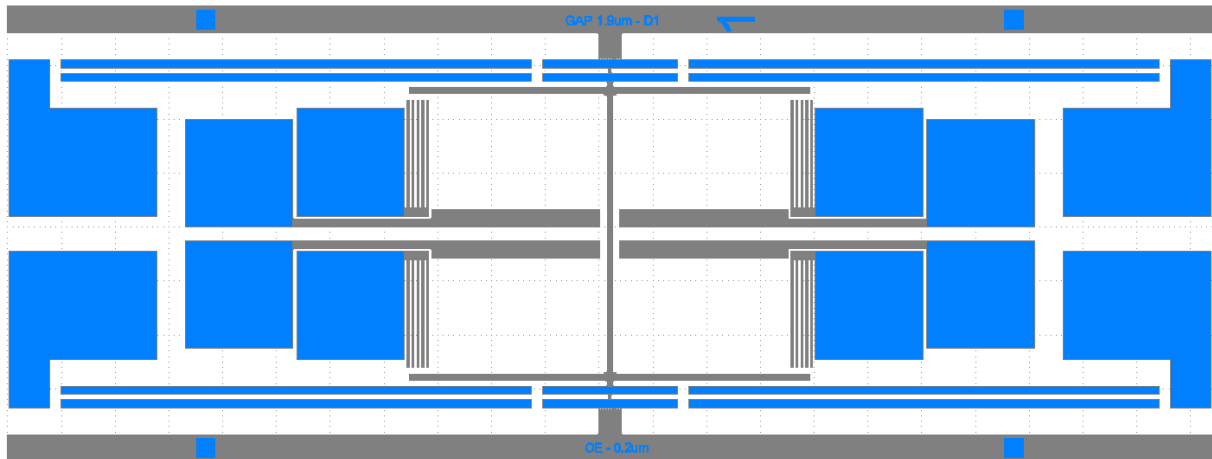


Figure 39. GS1 and METAL structure KLayout model.

5.4.5 TRENCH

Figure 40 shows the TRENCH design. The Trench represents the zones of the magnetometer that aren't structurally fixed. These are mostly attached to the movable structures of the magnetometer but also an area around the magnetometer so that the complete device can be detached. This layer is used on the backside of the wafer to be used on the backside lithography.

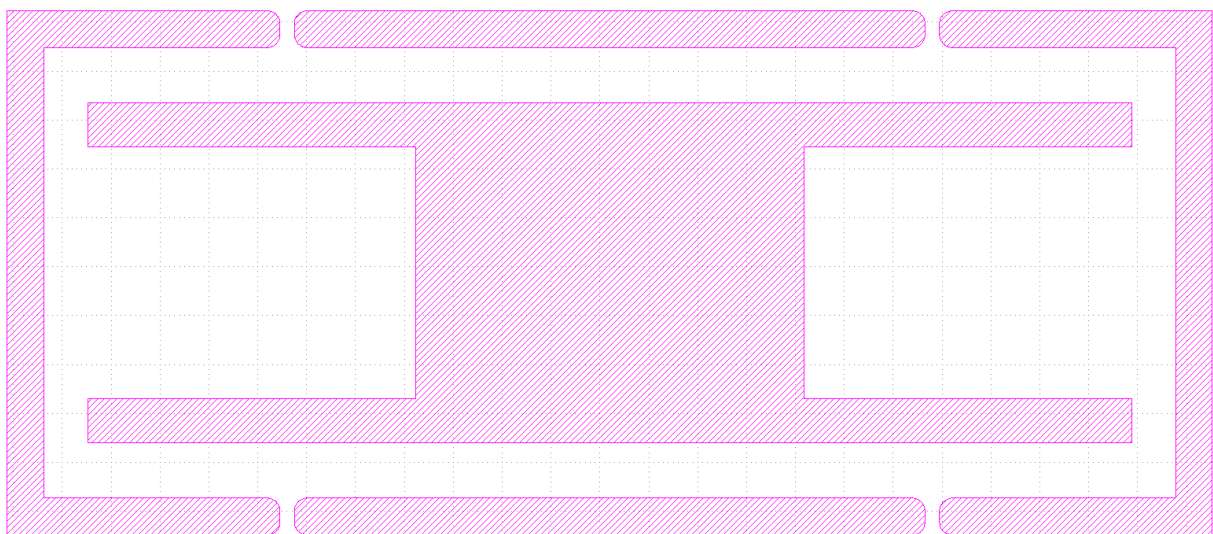


Figure 40. TRENCH structure KLayout Model.

5.4.6 Complete device

When all layers are added, the complete fabrication process design is assembled resulting in the magnetometer that was previously simulated. Figure 41 is a mashup of all the layers where it's shown the objective that each of these layers has.

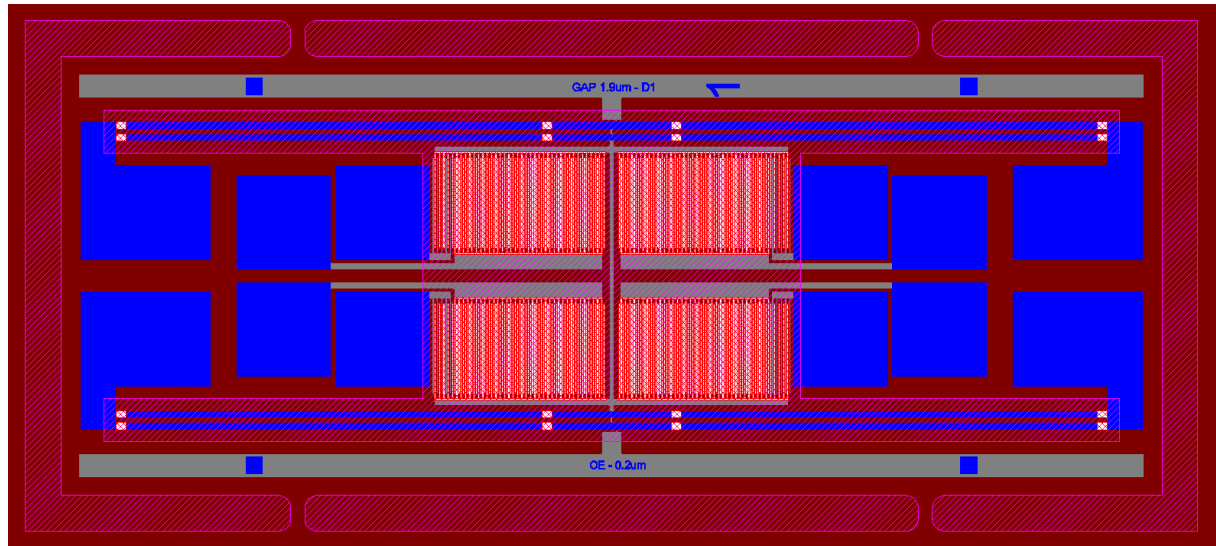


Figure 41. Complete structure layout.

5.4.7 Other structures

Complementary structures were also added. Figure 42 illustrates an example of these structures. On the left side, there are test structures that examine if the gap between the parallel plates is fully etched at the end of the frontside DRIE step by testing the impedance between both sides of the contacts. On the right side of the image, there are examples of the structures used for alignment verification between lithographies.

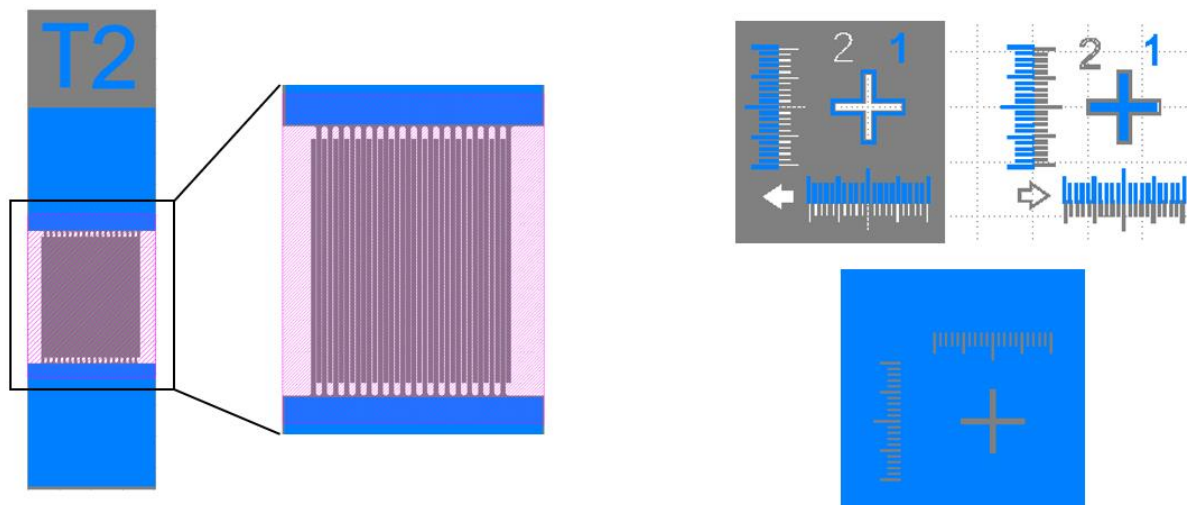


Figure 42. Parallel plate gap testing (left) and calibration (right) devices KLayout models.

As the fabrication methods aren't 100% reliable, several versions of the magnetometer and testing devices were constructed. This happens due to the etching of the silicon having the possibility of over-etching the parallel plates which implies that, if there is an over-etch of $0.1\mu\text{m}$, a $7\mu\text{m}$ wide parallel plate will have $6.9\mu\text{m}$ instead. To prevent this effect, an overextension was introduced to the width of the plates. The editions can be seen in table 15.

Table 15. Different device and test structures versions.

Device Version	Parallel Plate Gap (μm)	Overextension (μm)	Test Structure Version	Parallel Plate Gap (μm)
D1	1.9	0.2	T2	1.7
D2	1.9	0.1	T3	1.9
D3	1.9	0	T4	1.8
D4	1.8	0	T5	2
D5	2	0		

5.4.8 Complete wafer design

When taking into consideration the several designs proposed in this work, a unit can be conceived. Figure 43 shows the result of the addition of all editions of the magnetometer into a unit.

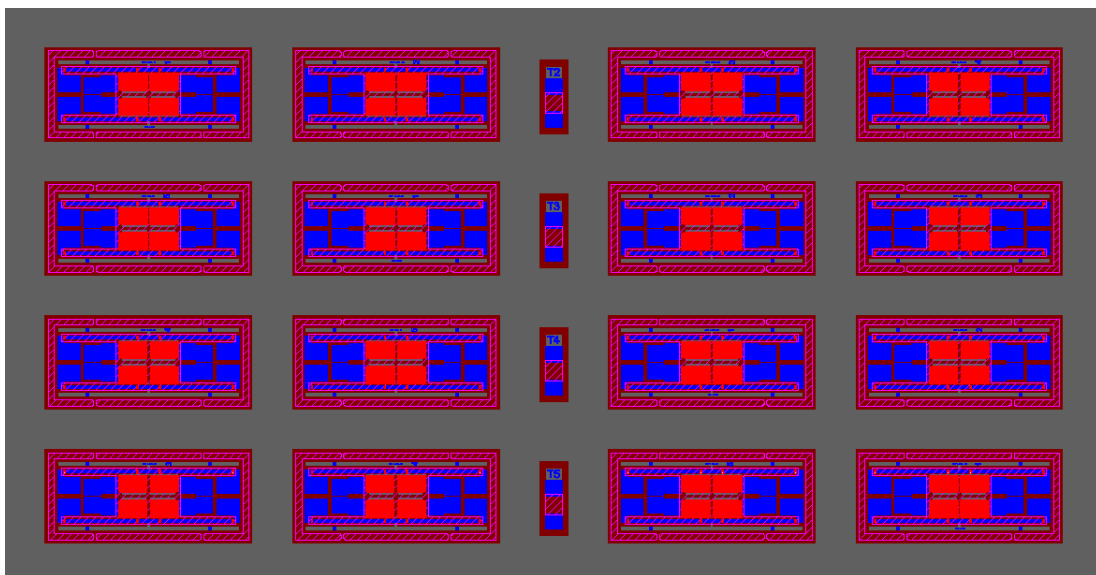


Figure 43. Single unit layout. All versions of the magnetometer and testing devices were assembled in a single unit so it can be replicated throughout the wafer.

Then each unit will be replicated until the full area of the wafer is filled. Three sections of alignment marks were also introduced in between units. An accelerometer design was also introduced to the units due to it sharing the same microfabrication process. Figure 44 shows the final result. A GS1 area expansion is necessary to define the square boundaries of the layer. On that topic, each mask had a $1\mu\text{m}^2$ square placed in each corner to define the borders.

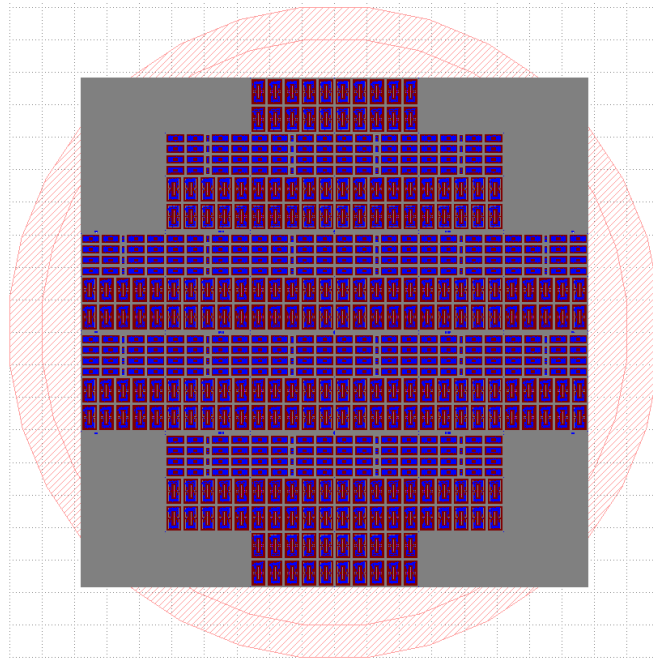


Figure 44. Final wafer layout.

5.5 Microfabrication results

Regarding the fabrication of the device, it was unfortunately not completed before the conclusion of this dissertation. Problems with a DWL malfunction and personal availability took a high toll on the time that was allocated for the microfabrication and characterization of the device. The fabrication process started with a successful frontside deposition and patterning of the metal layer. Figure 45 shows the result of deposition and patterning of photoresist where magnetometer versions 1 and 4 and an alignment mark can be seen.

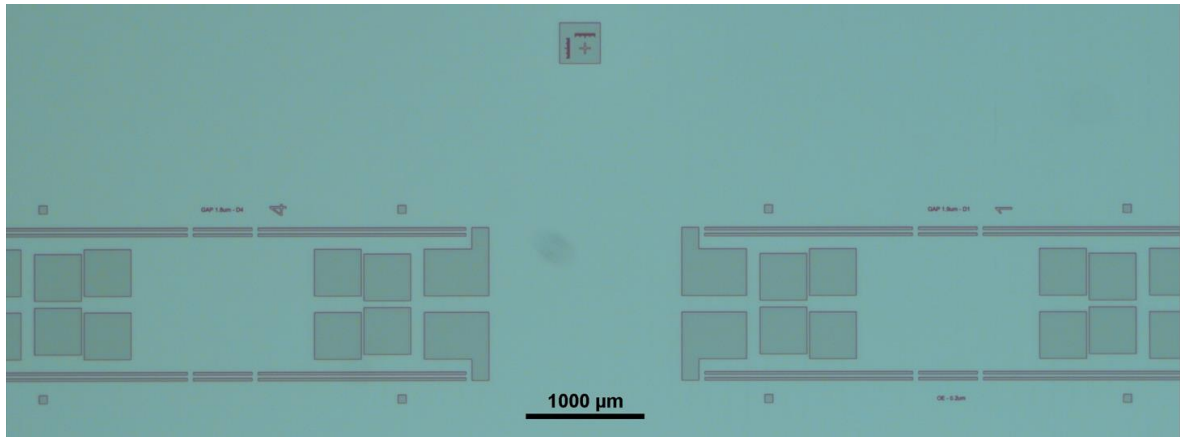


Figure 45. Photoresist deposition and patterning step results by optical microscope

After this came the chemical etching of the exposed metal. Figure 46 shows an image of the metal contacts and lever-like bars that were successfully etched. Some residue marks can be found in between the metal. Supposedly, this is due to a chemical reaction between the aluminium etchant and the AlSiCu where residues of silicon dioxide can be found. Finally, the wafer was, both frontside and backside, covered with SiO₂. This was the last step that was made in the INL cleanroom facilities (at the date of writing this thesis).

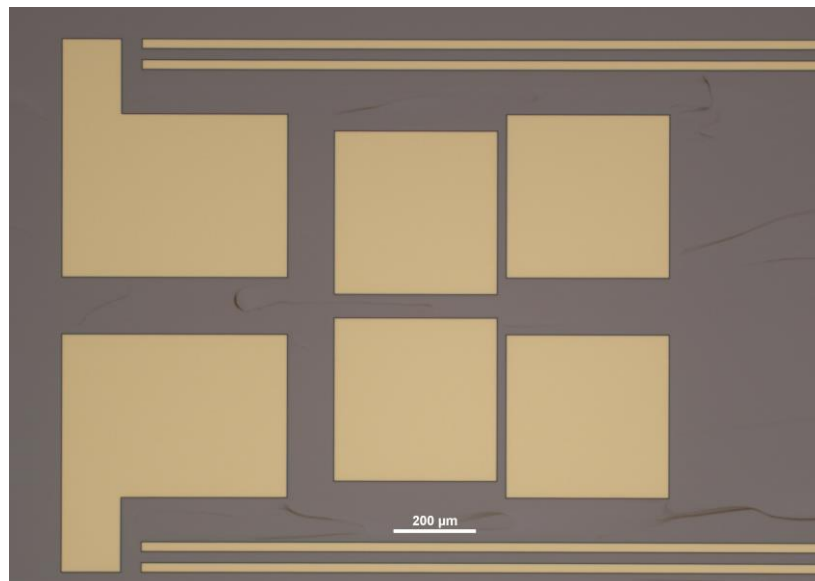


Figure 46. Magnetometer pads and lever-like bars after chemical etching by optical microscope.

6. CONCLUSION AND FUTURE WORK

In the present work, a successful design of a magnetometer theoretically capable of reaching all proposed objectives was achieved. The analytical models and FEM modelling approaches used are well established and have been used previously for similar devices, which grants a high level of confidence that the fabricated microstructures will be able to achieve the modelled performance. In the simulations, all parameters were attained, most of them even going over the prerequisites with special attention to the variation at the 20nT magnetic field where the magnetometer outperformed the 1aF barrier by 37% while maintaining the 50Hz bandwidth and 100Ω electrical resistance per current path. The thermomechanical noise was also well below the $3 \text{ nT}/\sqrt{\text{Hz}}$ limit at a staggering $1.77 \text{ nT}/\sqrt{\text{Hz}}$ which is a major improvement from the literature. The successful integration of INL manufacturing processes into the design was also an excellent achievement with successful KLayout masks adaptation to the magnetometer design.

The delays in the microfabrication run did not allow the accomplishment of final fabricated devices in the timeline of the dissertation. However, all initial steps of the fabrication were concluded with success showing good results in the taken images. The familiarization with the fabrication methods at INL was fulfilling in the sense that being able to study up-to-date MEMS fabrication principles is a huge gain for someone in the area. The opportunity to learn new simulation (such as COMSOL) and design (AutoCAD and KLayout) tools from some of the researchers at INL has proved an invaluable experience.

For future work, the finishing of the fabrication steps of the magnetometer is a must followed by its characterization to compare it with the results from the simulations. Depending on the findings certain adaptations may be necessary for this device to be integrated with the existing z-axis MEMS magnetometer (developed by Rosana Dias). If all fabrication results are positive, the assembly of a 3-axis magnetometer would be possible utilizing the Z-axis magnetometer from Rosana Dias and two magnetometers developed in this work with a 90° rotation between them since all fabrication steps between the two types of magnetometers are equal.

REFERENCES

- [1] L.-S. Yoo, J.-H. Lee, Y.-K. Lee, S.-K. Jung, and Y. Choi, "Application of a Drone Magnetometer System to Military Mine Detection in the Demilitarized Zone," *Sensors*, vol. 21, no. 9, 2021, doi: 10.3390/s21093175.
- [2] Siming Zuo *et al.*, *Integrated Pico-Tesla Resolution Magnetoresistive Sensors for Miniaturised Magnetomyography; Integrated Pico-Tesla Resolution Magnetoresistive Sensors for Miniaturised Magnetomyography*. 2020. doi: 10.0/Linux-x86_64.
- [3] J. S. Bennett *et al.*, "Precision magnetometers for aerospace applications: A review," *Sensors*, vol. 21, no. 16. MDPI, Aug. 02, 2021. doi: 10.3390/s21165568.
- [4] M. K. Mishra, V. Dubey, P. M. Mishra, and I. Khan, "MEMS Technology: A Review," *J. Eng. Res. Reports*, pp. 1–24, 2019, doi: 10.9734/jerr/2019/v4i116891.
- [5] A. S. Algamili *et al.*, "A Review of Actuation and Sensing Mechanisms in MEMS-Based Sensor Devices," *Nanoscale Res. Lett.*, vol. 16, no. 1, 2021, doi: 10.1186/s11671-021-03481-7.
- [6] J. Yunas *et al.*, "Polymer-Based MEMS electromagnetic actuator for biomedical application: A review," *Polymers (Basel)*, vol. 12, no. 5, 2020, doi: 10.3390/POLYM12051184.
- [7] P. Ragam and N. Devidas Sahebraoji, "Application of MEMS-based accelerometer wireless sensor systems for monitoring of blast-induced ground vibration and structural health: a review," *IET Wirel. Sens. Syst.*, vol. 9, no. 3, pp. 103–109, Jun. 2019, doi: <https://doi.org/10.1049/iet-wss.2018.5099>.
- [8] J. Ramakrishnan, P. T. R. Gaurav, N. S. Chandar, and N. M. Sudharsan, "Structural design, analysis and DOE of MEMS-based capacitive accelerometer for automotive airbag application," *Microsyst. Technol.*, vol. 27, no. 3, pp. 763–777, 2021, doi: 10.1007/s00542-020-04979-3.
- [9] EEHERALD, "Introduction and application areas for MEMS," *EEHERALD*, 2017. https://www.eeherald.com/section/design-guide/mems_application_introduction.html (accessed Jul. 28, 2022).
- [10] J. H. Rector, M. Slaman, R. Verdoold, D. Iannuzzi, and S. V. Beekmans, "Optimization of the batch production of silicon fiber-top MEMS devices," *J. Micromechanics Microengineering*, vol. 27, no. 11, 2017, doi: 10.1088/1361-6439/aa8c4e.
- [11] W. Niu *et al.*, "Summary of Research Status and Application of MEMS Accelerometers," *J. Comput. Commun.*, vol. 06, no. 12, pp. 215–221, 2018, doi: 10.4236/jcc.2018.612021.

- [12] X. Ren, X. Zhou, S. Yu, X. Wu, and D. Xiao, "Frequency-Modulated MEMS Gyroscopes: A Review," *IEEE Sens. J.*, vol. 21, no. 23, pp. 26426–26446, 2021, doi: 10.1109/JSEN.2021.3117939.
- [13] A. V. Ivanov and A. A. Zhilenkov, "The use of IMU MEMS-sensors for designing of motion capture system for control of robotic objects," *Proc. 2018 IEEE Conf. Russ. Young Res. Electr. Electron. Eng. EIconRus 2018*, vol. 2018-Janua, pp. 890–893, 2018, doi: 10.1109/EIconRus.2018.8317231.
- [14] M. Kok and T. B. Schön, "Maximum likelihood calibration of a magnetometer using inertial sensors," *IFAC Proc. Vol.*, vol. 47, no. 3, pp. 92–97, 2014, doi: <https://doi.org/10.3182/20140824-6-ZA-1003.02025>.
- [15] Q. Qixing, Y. Yanjuan, S. Zhaolong, and Z. Shoulong, "Research on the Z-axis Magnetic Sensor Based on the Giant Magnetoresistance Effect," in *2021 4th International Conference on Advanced Electronic Materials, Computers and Software Engineering (AEMCSE)*, 2021, pp. 229–232. doi: 10.1109/AEMCSE51986.2021.00055.
- [16] M. Oogane *et al.*, "Sub-pT magnetic field detection by tunnel magneto-resistive sensors," *Appl. Phys. Express*, vol. 14, no. 12, 2021, doi: 10.35848/1882-0786/ac3809.
- [17] C. Mauc, T. Perrier, R. Levy, J. Moulin, and P. Kayser, "Magnetometer based on a quartz MEMS resonator with two DETFs and a stack of magnetic materials," in *2022 IEEE International Symposium on Inertial Sensors and Systems (INERTIAL)*, 2022, pp. 1–4. doi: 10.1109/INERTIAL53425.2022.9787760.
- [18] W. Zhang and J. E.-Y. Lee, "Frequency-based magnetic field sensing using Lorentz force axial strain modulation in a double-ended tuning fork," *Sensors Actuators A Phys.*, vol. 211, pp. 145–152, 2014, doi: <https://doi.org/10.1016/j.sna.2014.01.022>.
- [19] M. Li, S. Sonmezoglu, and D. A. Horsley, "Extended Bandwidth Lorentz Force Magnetometer Based on Quadrature Frequency Modulation," *J. Microelectromechanical Syst.*, vol. 24, no. 2, pp. 333–342, 2015, doi: 10.1109/JMEMS.2014.2330055.
- [20] P. J. Baxandall, "Noise_in_Transistor_Circuits," *Wirel. World*, pp. 1–11, 2013, [Online]. Available: <papers://b601f53a-84e1-4f0c-abd7-620bc101dbfb/Paper/p6948>
- [21] S. Shao, A. Gao, Y. Wang, and T. Wu, "Wide Bandwidth Lorentz-Force Magnetometer Based on Lateral Overtone Bulk Acoustic Resonator," in *2021 IEEE 34th International Conference on Micro Electro Mechanical Systems (MEMS)*, 2021, pp. 879–882. doi: 10.1109/MEMS51782.2021.9375335.
- [22] M. Kahr, W. Hortschitz, H. Steiner, M. Stifter, A. Kainz, and F. Keplinger, "Novel 3D-Printed MEMS

- Magnetometer with Optical Detection,” *Proceedings*, vol. 2, no. 13, 2018, doi: 10.3390/proceedings2130783.
- [23] L. Zhang, T. Tsukamoto, and S. Tanaka, “Frequency Modulated MEMS Lorentz Force Magnetometer Using CW/CCW Modes,” in *2022 IEEE International Symposium on Inertial Sensors and Systems (INERTIAL)*, 2022, pp. 1–4. doi: 10.1109/INERTIAL53425.2022.9787717.
- [24] X. Song *et al.*, “A MEMS Resonant Lorentz-Force Magnetometer with Both Structural Topology Optimization and Parametric Pumping for Q-Factor Enhancement,” in *2022 IEEE 35th International Conference on Micro Electro Mechanical Systems Conference (MEMS)*, 2022, pp. 947–950. doi: 10.1109/MEMS51670.2022.9699520.
- [25] V. Kumar, A. Ramezany, M. Mahdavi, and S. Pourkamali, “Amplitude modulated Lorentz force MEMS magnetometer with picotesla sensitivity,” *J. Micromechanics Microengineering*, vol. 26, no. 10, 2016, doi: 10.1088/0960-1317/26/10/105021.
- [26] Aditi, S. Das, P. Kothari, S. Das, and R. Gopal, “Dual-axis Lorentz Force MEMS Magnetometer,” *2020 IEEE Sensors Appl. Symp. SAS 2020 - Proc.*, pp. 2020–2023, 2020, doi: 10.1109/SAS48726.2020.9220035.
- [27] G. Langfelder, G. Laghi, P. Minotti, A. Tocchio, and A. Longoni, “Off-resonance low-pressure operation of lorentz force MEMS magnetometers,” *IEEE Trans. Ind. Electron.*, vol. 61, no. 12, pp. 7124–7130, Dec. 2014, doi: 10.1109/TIE.2014.2317153.
- [28] Rosana A. Dias, Eurico E. Moreira, and Filipe S. Alves, *2020 IEEE 33rd International Conference on Micro Electro Mechanical Systems (MEMS)*. IEEE, 2020.
- [29] P. Ripka and M. Janosek, “Advances in Magnetic Field Sensors,” *IEEE Sens. J.*, vol. 10, no. 6, pp. 1108–1116, 2010, doi: 10.1109/JSEN.2010.2043429.
- [30] J. Javor, A. Stange, C. Pollock, N. Fuhr, and D. Bishop, *100pTcm Sensitive MEMS Resonant Magnetometer from a Commercial Accelerometer*. 2019.
- [31] D. Novotny, V. Petrucha, M. Dressler, and A. Platil, “Characterization of a Digital AMR Magnetometer for Space Applications,” *IEEE Trans. Instrum. Meas.*, vol. 70, 2021, doi: 10.1109/TIM.2020.3043867.
- [32] G. He *et al.*, “PicoTesla magnetic tunneling junction sensors integrated with double staged magnetic flux concentrators,” *Appl. Phys. Lett.*, vol. 113, no. 24, pp. 1–6, 2018, doi: 10.1063/1.5052355.
- [33] E. Y. Tsymbal and D. G. Pettifor, “ChemInform Abstract: Perspectives of Giant

- Magnetoresistance.,” *ChemInform*, vol. 33, no. 4, pp. 113–no, 2010, doi: 10.1002/chin.200204255.
- [34] C. Muşuroi, M. Oproiu, M. Volmer, and I. Firastrau, “High Sensitivity Differential Giant Magnetoresistance (GMR) Based Sensor for Non-Contacting DC/AC Current Measurement.,” *Sensors (Basel)*, vol. 20, no. 1, Jan. 2020, doi: 10.3390/s20010323.
- [35] H. Nhalil *et al.*, “Planar Hall Effect Magnetometer with 5 pT Resolution,” *IEEE Sensors Lett.*, vol. 3, no. 12, pp. 10–13, 2019, doi: 10.1109/LSENS.2019.2947681.
- [36] Supracon, “How does a SQUID sensor work?,” *Supracon*. <http://www.supracon.com/cms/html/2/browse/232#n1> (accessed Aug. 29, 2022).
- [37] Z. Wang *et al.*, “Highly Sensitive Flexible Magnetic Sensor Based on Anisotropic Magnetoresistance Effect,” *Adv. Mater.*, vol. 28, no. 42, pp. 9370–9377, 2016, doi: 10.1002/adma.201602910.
- [38] A. Guedes, R. Macedo, G. Jaramillo, S. Cardoso, P. P. Freitas, and D. A. Horsley, “Hybrid GMR sensor detecting 950 pT/sqrt(Hz) at 1 hz and room temperature,” *Sensors (Switzerland)*, vol. 18, no. 3, pp. 1–8, 2018, doi: 10.3390/s18030790.
- [39] X. Zhang *et al.*, “Fabrication and measurement of Nb-based SQUID magnetometer,” *Phys. C Supercond. its Appl.*, vol. 548, pp. 1–4, 2018, doi: 10.1016/j.physc.2018.01.016.
- [40] M. J. Thompson and D. A. Horsley, “Parametrically Amplified Z -Axis,” *Jmems*, vol. 20, no. 3, pp. 702–710, 2011.
- [41] V. Kempe, *Inertial MEMS: principles and practice*. Cambridge University Press, 2011.
- [42] A. Ramanan, Y. X. Teoh, W. Ma, and W. Ye, “Characterization of a laterally oscillating microresonator operating in the nonlinear region,” *Micromachines*, vol. 7, no. 8, 2016, doi: 10.3390/mi7080132.
- [43] T. R. Kuphalat, “Q AND BANDWIDTH OF A RESONANT CIRCUIT,” in *Lessons In Eletric Circuits*, Sixth., 2007, pp. 147–148. [Online]. Available: <https://www.allaboutcircuits.com/assets/pdf/alternating-current.pdf>
- [44] D. C. Hovde, M. D. Prouty, I. Hrvoic, and R. E. Slocum, “Commercial magnetometers and their application,” in *Optical Magnetometry*, D. F. Jackson Kimball and D. Budker, Eds. Cambridge: Cambridge University Press, 2013, pp. 387–405. doi: DOI: 10.1017/CBO9780511846380.021.
- [45] G. Langfelder and A. Tocchio, “Operation of Lorentz-force MEMS magnetometers with a frequency offset between driving current and mechanical resonance,” *IEEE Trans. Magn.*, vol. 50, no. 1, 2014, doi: 10.1109/TMAG.2013.2281404.

- [46] V. Lindroos, "Gas Damping in Vibrating MEMS structures," in *Handbook of silicon based MEMS materials and technologies*, First., J. Ramsden, Ed. William Andrew/Elsevier, 2010, pp. 276–285.
- [47] K. C. D. Hickman, "Scientific Foundations of Vacuum Technique. Saul Dushman. New York: John Wiley; London: Chapman & Hall, 1949. Pp. xi +882. (Illustrated.) \$15.00.," *Science (80-)*, vol. 109, no. 2834, p. 407, Apr. 1949, doi: 10.1126/science.109.2834.407.a.
- [48] T. Veijola and M. Turowski, "Compact damping models for laterally moving microstructures with gas-rarefaction effects," *J. Microelectromechanical Syst.*, vol. 10, no. 2, pp. 263–273, Jun. 2001, doi: 10.1109/84.925777.
- [49] COMSOL, "Introduction to Eigenfrequency Analysis," *COMSOL*, 2018. <https://www.comsol.com/multiphysics/eigenfrequency-analysis> (accessed Aug. 31, 2022).
- [50] N. Kumar, *Comprehensive physics XII*. Laxmi Publications, 2004. [Online]. Available: https://books.google.pt/books?hl=pt-BR&lr=&id=IryMtwHHnglC&oi=fnd&pg=PR8&dq=Comprehensive+Physics+XII&ots=sA0kheKrcz&sig=wpNMIUWUXWycy5BHbfl5a4D2X8w&redir_esc=y#v=onepage&q=Comprehensive Physics XII&f=false
- [51] J. Mitchell, H. D. Griffiths, and I. Boyd, "Sir John Ambrose Fleming–His involvement in the development of wireless." Chap, 2006.
- [52] Clean-rooms, "ISO Cleanroom Standards," *Clean-rooms.org*. <https://www.clean-rooms.org/iso-cleanroom-standards/> (accessed Sep. 29, 2022).
- [53] E. Akçah, K. Nemoto, and R. Uzsoy, "Cycle-time improvements for photolithography process in semiconductor manufacturing," *IEEE Trans. Semicond. Manuf.*, vol. 14, no. 1, pp. 48–56, 2001, doi: 10.1109/66.909654.
- [54] I. V. Tudose *et al.*, "Chapter 2 - Chemical and physical methods for multifunctional nanostructured interface fabrication," in *Micro and Nano Technologies*, V. Dinca and M. P. B. T.-F. N. I. for E. and B. A. Sucheai, Eds. Elsevier, 2019, pp. 15–26. doi: <https://doi.org/10.1016/B978-0-12-814401-5.00002-5>.
- [55] R. Kumar and Kamakshi, "2 - Synthesis routes of ZnO nanocrystallites," in *Metal Oxides*, K. B. T.-N. Z. O. Awasthi, Ed. Elsevier, 2021, pp. 23–56. doi: <https://doi.org/10.1016/B978-0-12-818900-9.00012-7>.
- [56] D. Vacuum, "Discovery," *Denton Vacuum*, 2022. <https://www.dentonvacuum.com/products/discovery/> (accessed Sep. 29, 2022).
- [57] Avantor, "Aluminum etch 16:1:1:2," *Avantor*, 2022.

- <https://us.vwr.com/store/product/18918095/aluminum-etch-16-1-1-2> (accessed Sep. 29, 2022).
- [58] J. Loomis, K. M. Walsh, J. Loomis, D. Ratnayake, C. McKenna, and K. M. Walsh, "Grayscale lithography — automated mask generation for complex three- dimensional topography," vol. 15, no. 1, 2022, doi: 10.1117/1.JMM.15.1.
- [59] I. S. Garcia *et al.*, "Fabrication of a MEMS Micromirror Based on Bulk Silicon Micromachining Combined with Grayscale Lithography," *J. Microelectromechanical Syst.*, vol. 29, no. 5, pp. 734–740, 2020, doi: 10.1109/JMEMS.2020.3006746.
- [60] B. J. Jones and N. Nelson, "Sticking non-stick: Surface and Structure control of Diamond-like Carbon in Plasma Enhanced Chemical Vapour Deposition," *J. Phys. Conf. Ser.*, vol. 768, no. 1, 2016, doi: 10.1088/1742-6596/768/1/012011.
- [61] M. Hughes, "What is Plasma Enhanced Chemical Vapor Deposition (PECVD)?," *Semicore*, 2022. <https://www.semicore.com/news/118-what-is-plasma-enhanced-chemical-vapor-deposition-pecvd> (accessed Sep. 28, 2022).
- [62] F. Karouta, "A practical approach to reactive ion etching," *J. Phys. D. Appl. Phys.*, vol. 47, no. 23, 2014, doi: 10.1088/0022-3727/47/23/233501.
- [63] H. V. Jansen, M. J. De Boer, S. Unnikrishnan, M. C. Louwerse, and M. C. Elwenspoek, "Black silicon method X: A review on high speed and selective plasma etching of silicon with profile control: An in-depth comparison between Bosch and cryostat DRIE processes as a roadmap to next generation equipment," *J. Micromechanics Microengineering*, vol. 19, no. 3, 2009, doi: 10.1088/0960-1317/19/3/033001.
- [64] F. Laermer, A. Schilp, and Robert Bosch GmbH, "Method of anisotropically etching silicon," *US Pat. 5501893*, p. US5501893 A, 1993, [Online]. Available: <https://patents.google.com/patent/US5501893A/en>
- [65] P. Cycle, "What is the Bosch Process?," pp. 1–6, 2020, [Online]. Available: <https://www.samco.co.jp/en/technews/2020/what-is-the-bosch-process.php>
- [66] INL, "MNF_Timaris FTM - TiW, AlSiCu and Al₂O₃ sputtering," *INL*. <https://lims.inl.int/WebForms/Equipment/EquipmentView.aspx?toolId=31> (accessed Sep. 14, 2022).
- [67] INL, "MNF_Suss Optical Resist Track," *INL*. <https://lims.inl.int/WebForms/Equipment/EquipmentView.aspx?toolId=23> (accessed Sep. 14, 2022).

- [68] INL, "MNF_DWL Direct Write Laser Lithography," *INL*.
- [69] INL, "MNF_Wet bench 4," *INL*.
<https://lims.inl.int/WebForms/Equipment/EquipmentView.aspx?toolId=47> (accessed Sep. 14, 2022).
- [70] INL, "MNF_PVA TEPLA Plasma Asher_1," *INL*.
<https://lims.inl.int/WebForms/Equipment/EquipmentView.aspx?toolId=32> (accessed Sep. 14, 2022).
- [71] INL, "MNF_SPTS PECVD," *INL*.
<https://lims.inl.int/WebForms/Equipment/EquipmentView.aspx?toolId=66>
- [72] INL, "MNF_SPTS APS - SiO2 Etcher," *INL*.
<https://lims.inl.int/WebForms/Equipment/EquipmentView.aspx?toolId=18> (accessed Sep. 15, 2022).
- [73] INL, "MNF_SPTS Pegasus," *INL*.
<https://lims.inl.int/WebForms/Equipment/EquipmentView.aspx?toolId=35> (accessed Sep. 15, 2022).

ANNEX I – MATLAB ALGORITHM

In the simulation stage, a mixture of COMSOL and MATLAB was used to simulate the best structural combination for the magnetometer. Figure 47 shows the universal constants that were used throughout the work.

```
%-----Constant parameters-----
E_young=1.69e11;%Young's modulus
T=300;
C_air=112;%K, air Sutherland constant, Lindroos handbook of mems
kB=1.38e-23;%Boltzmann's constant
E0=8.8546e-12;
NA=6.02214e23;%Avogadro number
mm=28.97e-3/NA;%air molecular mass=28.97kg/kmol=28.97e-3kg/mol
rhoSi=2329;%density silicon
rhoAl=2710;%density Aliminium
erhoSi=1.5e-4;%Electrical resistance/resistivity Silicon
erhoAl=28.2e-9;%Electrical resistance/resistivity Aluminium
eta_airrl=17.22e-6;%dynamic viscosity 17.22 ?Pa s @0Å°C and 1bar
eta_air=eta_airrl*(273.15+C_air)/(T+C_air)*(T/273.15)^(3/2); %at 1BAR

%-----Operation conditions: pressure and current-----
P=1.01*10e5;%10mbar=1000Pa
P=100;
lambda=69e-9*101.3e3/P;%mean fre path
I=4e-3;%4mA current
```

Figure 47. MATLAB constants and parameters.

Figure 48 represents the geometrical parameters that composed the magnetometer structure.

```
%-----Geometrical parameters-----
h=;%silicon thickness
hAl=;%Aluminum thickness
nlz=;%number of complete structures

%Structure 1 - Barra de lorentz
lLz=;%Lz bar length
wLz=;%Lz bar width
hLz=h;%Height = silicon thickness

%Structure 2 - Lever-like bar
lLever=;%Lever-like bar length
wLever=;%Lever-like width
hLever=h;%Height = silicon thickness

%Structure 3 - Spring bar
ls=;%Spring bar length
ws=;%Spring bar width
hs=;%Spring bar height

%Capacitor
ld=;%Capacitor superposition (Movable Plate // Fixed Plate)
lPlate=ld+20e-6;%length Capacitor Plate
wPlate=;%width Capacitor Plate
hPlate=;%hight Plate
d1=;%initial gap
d2=;%second gap
np_ml=;%number of dampers movable single sided
np_fl=np_ml+2;
nd=2*np_ml;%Total number of dampers
%Total number of fingers/plates = nd+2 or nd+4

%Capacitor Suport
lcs=(2*wPlate+d1+d2)*np_ml;%length capacitor support
wcs=;
hcs=h;
%Capacitor Bar
lb=;% 2*lPlate + sobra para as placas do condensador caberem sem entrar em contacto
wb=;
hb=h;
%Initially the structure has 1 Lz bar, 2 lever-like bars, 4 spring bars
```

Figure 48. MATLAB geometrical Parameters.

Figure 49 demonstrates the electrical and mass parameters of the magnetometer.

```
%-----Electrical resistance -----
%Current path resistance
Rl1z=(erhoAl*1Lz)/(hAl*(wLz-6e-6));%Lorentz bar resistance (rho*L/Area (Al width taken in consideration)
Rl1=(erhoAl*1Lever)/(hAl*(wLever-6e-6));%Lever-like bar resistance (rho*L/Area (Al width taken in consideration)
RS=erhoSi*ls/(hs*ws);%Spring bar resistance(rho*L/Area)
R=Rl1z+2*Rl1 + 4*RS; %resistance per current path

%-----Mass-----
%Bars Silicon Volume
VSiLz=1Lz*wLz*h; %Structure 1 volume
VSiLeverLike=1Lever*wLever*h; %Structure 2 volume
VSiSpring=ls*ws*hs; %Structure 3 volume
%Capacitor Volume
Vparallel_plate=(np_ml+np_mr)*1Plate*wPlate*hs; %Parallel Plate volume
Vcapacitor_supp=lcs*wcs*hcs;
Vcapacitor_bar= lb*wb*hb;
%Bars Aliminium Volume
VAl=hAl*(wLz-6e-6)*(2*1Lever+1Lz);%Volume Al - Only the lorentz and lever-like bars have aluminium
%Total Volume - VCapacitor
VtotalSi=4*VSiSpring+2*VSiLeverLike+VSiLz; %Total volume Silicon Current carrying bar
%Mass density*volume
m_total=nlz*(rhoSi*VtotalSi+VAl*rhoAl)+(Vparallel_plate+Vcapacitor_supp+Vcapacitor_bar)*rhoSi;
m_central=nlz*(rhoSi*VSiLz+hAl*(wLz-6e-6)*(1Lz)*rhoAl)+(Vparallel_plate+Vcapacitor_supp+Vcapacitor_bar)*rhoSi;
```

Figure 49. MATLAB electrical and mass parameters.

Figure 50 shows the slide-damping model with the Veijola et al. adaptation to the Q_{pr} model.

```
%-----SLIDE DAMPING-----
%Veijola04 squeeze with inertia,elongations,compressibility and rarefaction
%geometry parameters
wd=hPlate;%width damper (=SOI height)

Kn=1.016*lambda/dl;%Knudsen number;

dl=dl/(1+8.5*dl/wd);%elongation according to lindroos/Veijola
Qpr_s=1+2*Kn+0.2*(Kn)^0.788*exp(-Kn/10);%Relative flowrate coefficient || Eq pag 267 - LINDROOS/2010
bslide=eta_air*wd*ld/(Qpr_s*dl);%effective viscosity

%Fdamping=-bslide*v0;
b=nd*bslide
```

Figure 50. MATLAB slide damping model.

Figure 51 shows some of the tried mechanical stiffness models and the COMSOL entries at the end.

```
%-----Mechanical stiffness-----
% kcantconc=3*E*I/(ls)^3;
% kcantdistr=8*E*I/ls^4;
% kguidconc=12*E*I/(ls)^3;
% kbridgeconc=192*E*I/(ls^2)^3
%STIFNESS CLAMO-GUIDED
% Is=1/12*ws*hs^3;%area moment of inertia
% kmola=12*Is*E_young/((ls)^3)
% k1=nlz*2*12*Is*E_young/((2*ls)^3)%total stiffness based on clamped-guided beam stiffness;
%
% FL=nlz*I*lc*(amp_B+cte_B); %in N or N/sqrt(Hz)...
% FL=1e-12
% keq=k1;
% xeq=FL/keq;
% %xreal=xeq+1Lever*sind(teta)
% %FLz=5e-13;
% L=1Lever; %ou lb*2?
% max_def=FL*L^2./(6*E_young*I).*(2*L); %verificar se este 2 vem da eq ou é já a transformar lcant em length_guided
% max_der=(FL*L^2./(6*E_young*I).*(2*L)-FL.*(L-1e-9).^2./(6*E_young*I).*(3*L-(L-1e-9)))/1e-9;
% max_teta=atand(max_der);
% xreal=xeq+1Lever*sind(max_teta);
% k=FL/xreal
k_conc=28;%comsol simulation result for concentrated force
k_dist=52;%comsol simulation result for distributed force
```

Figure 51. MATLAB mechanical stiffness models.

Figure 52 demonstrates some of the natural frequency and Q-factor simulations that were tried before the introduction of the COMSOL simulations.

```
%-----Mechanical parameters-----
f0=sqrt(k_conc/m_total)/(2*pi)%Resonance frequency
f0_conc=sqrt(k_conc/m_central)/(2*pi) %Resonance frequency; choose whichever is closer to comsol f0
f0_central=(f0+f0_conc)/2
f0_sim=4977;
fst_eingen=4977;
closest_eigen=8636;
%Q=sqrt(k_conc*m_total)/b; %Quality factor
%Q_conc=sqrt(k_conc*m_central)/b %Quality factor; choose the chosen for f0
%Q_calc= (Q+Q_central)/2

m_eff_conc=k_conc/(2*pi*f0_sim)^2
m_eff_dist=k_dist/(2*pi*f0_sim)^2
Q_conc=sqrt(k_conc*m_eff_conc)/b
%Q_eff_dist=sqrt(k_dist*m_eff_dist)/b
```

Figure 52. MATLAB resonance frequency and Q-factor simulations.

Figure 53 reveals some of the experimental parameters and equations in the Lorentz-force intensity calculus.

```
B_AC=0;%valor de pico, AC component of magfield
B_DC=20e-9; %DC component of magfield4984.5
%B_DC=60e-6;
fB=50;%magnetic field frequency
%fnnoise=15e3;%not used
%nst=1/(2*fnnoise);%gera ruido na banda fnnoise. afrequencia dos valores Ã© fnnoise*2
% amp_noise=fnnoise*sqrt(fnnoise);%unidades Newton
% ampnoise=1e-40;
%fcut=1000;
%simf=1e-40;
df=f0_sim-4952; %offset/desvio de frequencia relativamente Ã resonancia
%df=22;
%fil=f0_central-df;%frequencia de excitaÃ§Ã£o
fil=f0_sim-df;
noise=sqrt(4*kB*T*b)/(nlz*I*lc)%brownian noise/thermomechanical noise formula T/sqrt(Hz)
Tcarrier_ms=1/f0_sim*1000; %periodo
xi=0;
amp_il=nlz*I*lc;%valor de pico (pico-a-pico Ã© o dobro)
```

Figure 53. MATLAB Lorentz force.

```

%-----Simulation-----
FLz=nlz*I*lc*(B_DC+B_AC*sin(2*pi*fB))
% FLz=1e-12;%comsol simulation
%Displacement
xmax=FLz/k_dist
xmax_Q=Q_conc*xmax;
%Capacitance
C0=(2*np_ml*E0*ld*hPlate)/dl %C0_l=C0_r=C0
Cl_Q=(2*np_ml*E0*ld*(hPlate-xmax_Q))/dl;
Cr_Q=(2*np_mr*E0*ld*(hPlate-xmax_Q))/dl;
dC_Q=C0-Cr_Q
dC_af=dC_Q*1e18;
xmax_Q_nm=xmax_Q*1e9;
dCmax_Q_aF=dC_Q*1e18;%3.4e-21=zeptofarads :s
carriergain=1;
% Vmaxexp=dC*10e-3/1e-15*carriergain;
noise_expected=[num2str(noise) ' N/sqHz'];
noise_expected=[num2str(noise/(nlz*I*lc)) ' T/sqHz'];
noise_expected50Hz=[num2str(noise/(nlz*I*lc)*sqrt(50)) ' T'];
% xmax=200*6*4e-3*4e-3*64e-6/30; %xmax=Q*nlzIlB/k
BW_Q=f0_sim/Q_conc
d=1/(2*Q_conc);
fd=fil;
Mag=-10.*log10(1-2*(1-2*d.^2).*(fd./f0_sim).^2+(fd./f0_sim).^4);
Qeff=10.^(Mag./20)
BW_Qeff=f0_sim/Qeff
xmax_Qeff=Qeff*FLz/k_dist
Cl_Qeff=(2*np_ml*E0*ld*(hPlate-xmax_Qeff))/dl;
Cr_Qeff=(2*np_mr*E0*ld*(hPlate-xmax_Qeff))/dl;
dCmax_Qeff_aF=(C0-Cr_Qeff)*1e18
% Vmaxexpeff=(C0-Cr_eff)*10e-3/1e-15*carriergain;

```

Figure 55 shows one of the many Excel simulation sheets

[illegible]

67

ANNEX II – RUNSHEET

Figure 56 shows the 5 segments of production explained in chapter 5 in the runsheet format that was used as a guideline in the formulation of the fabrication steps of the magnetometer. The five steps are each divided into their excel sheet so the process can be more easily accompanied.

1- AlSiCu+SiO₂dep	2-FS GS HM pat	3-BS HM pat	4-FS GS DRIE	5-BS DRIE+Release
-------------------------------------	----------------	-------------	--------------	-------------------

Figure 56. Five-step fabrication process runsheet pages.

As the runsheets were too big to be put in the abstract and some of the process descriptions were INL properties a compilation of the steps was collected to represent each segment of the runsheet.

Frontside metal deposition and patterning followed by SiO₂ deposition:

1. SOI Substrate.
2. Pre-etch and Sputter Deposit (TiW/AlSiCu/Al₂O₃).
3. Frontside Lithography. Subdivided in vapor prime, spin coating, exposure, development, and optical inspection.
4. AlSiCu wet etch. Subdivided in wet aluminium etch and optical inspection.
5. Plasma asher.
6. PECVD HF-SiO₂ and wafer bow measurement.

Frontside Grayscale lithography and SiO₂ etch:

1. Backside Lithography. Subdivided in vapor prime, spin coating, exposure, development and optical inspection.
2. Frontside parallel step GS hard-mask patterning. Subdivided in APS RIE SiO₂ etch, optical inspection and reflectometry thin film thickness measurement. Step1.
3. Parallel step frontside GS resist thinning. Subdivided in PEG O₂ resist strip, optical inspection, and reflectometry thin film thickness measurement.
4. Parallel step frontside GS hard-mask patterning. Subdivided in APS RIE SiO₂ etch, optical inspection and reflectometry thin film thickness measurement.
5. Plasma Asher.

Backside Lithography and SiO₂ etch:

1. Frontside lithography. Subdivided in vapor prime, spin coating, exposure, development, and optical inspection.
2. Backside lithography. Subdivided in exposure, development, and optical inspection.
3. APS RIE SiO₂ etch.
4. Optical inspection.
5. Plasma asher.

Frontside Silicon Etch:

1. Parallel Step GS Si etch frontside. Subdivided in PEG RIE, optical inspection, and optical profilometer.
2. Parallel step GS hard-mask thinning correction. Subdivided in APS RIE SiO₂ etch, interferometer thickness measurement, and optical inspection.
3. Wafer cleaning. Subdivided in plasma asher, EKC cleaning, and plasma asher.
4. Parallel step GS Si etch frontside. Subdivided in PEG RIE, optical inspection, and optical profilometer.
5. PEG RIE.
6. Electrical measurement.

Backside Silicon Etch and structural release:

1. WAX mounting.
2. PEG RIE.
3. WAX demounting.
4. Plasma asher.
5. HF Vapour etch.
6. Optical inspection.